Journal Pre-proof

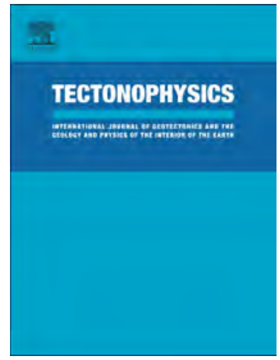


# Analogue modelling of marginal flexure in Afar, East Africa: Implications for passive margin formation

Frank Zwaan, Giacomo Corti, Derek Keir, Federico Sani

PII: S0040-1951(20)30278-X

DOI: https://doi.org/10.1016/j.tecto.2020.228595

Reference: TECTO 228595

To appear in: *Tectonophysics*

Received date: 27 April 2020

Revised date: 12 August 2020

Accepted date: 18 August 2020

Please cite this article as: F. Zwaan, G. Corti, D. Keir, et al., Analogue modelling of marginal flexure in Afar, East Africa: Implications for passive margin formation, *Tectonophysics* (2019), https://doi.org/10.1016/j.tecto.2020.228595

# Analogue modelling of marginal flexure in Afar, East Africa: implications for passive margin formation

Frank Zwaan[1,2], Giacomo Corti[3], Derek Keir[1,4], Federico Sani[1]

1) Dipartimento di Scienze della Terra, Università degli Studi di Firenze, Via la Pira 4, 50121 Florence, Italy
2) Institute of Geological Sciences, University of Bern, Baltzerstrasse 1+3, 3012 Bern, Switzerland
3) Consiglio Nazionale delle Ricerche, Istituto di Geoscienze e Georisorse, Via G. La Pira, 4, 50121 Florence, Italy
4) School of Ocean and Earth Science, University of Southampton, Southampton SO14 3ZH, UK

frank.zwaan@geo.unibe.ch, fzwaan@hotmail.com

**Keywords:** Crustal flexure; rifting; passive margin; continental break-up; marginal graben; magma-rich passive margin

**Abstract**

The Afar region in East Africa is a key locality for studying continental break-up. Within Afar proper, passive margins are developing, of which the Southern Afar Margin (SAM) contains synthetic (basinward) faulting, whereas crustal flexure, antithetic faulting and marginal grabens occur along the Western Afar Margin (WAM). Numerous conflicting scenarios for the evolution of the WAM exist. In this analogue modelling study we test various factors that may affect the development of a WAM-style passive margin: brittle crustal thickness, (en echelon) rheological contrasts, sedimentation and oblique extension.

Our experimental results illustrate how marginal flexure due to a weak lower crust below Afar elegantly reproduces the structural features of the WAM. Brittle crustal thickness controls what structures occur: a thinner brittle crust accommodates flexure internally, whereas increasing brittle thicknesses lead to faulting. Large escarpment faults develop early on, followed by late-stage antithetic faulting and marginal grabens. A thicker brittle crust also causes more subsidence, and higher strength contrasts between lower crustal domains leads to more localized deformation. Basin-wide sedimentation causes enhanced subsidence, as well as longer activity along large (escarpment) faults. Finally, oblique extension clearly prevents the development of marginal grabens, which only form in near-orthogonal extension.

These results support a tectonic scenario involving initial oblique extension due to Arabian plate motion, creating echelon synthetic escarpment faults along the WAM. After the Danakil Block started its independent rotation, near-orthogonal extension conditions occurred, allowing (enhanced) marginal flexure, antithetic faulting and marginal graben formation along the older en echelon escarpment. Differences in extension obliquity may also explain the differences in structural architectures between the WAM and SAM. The characteristics of the WAM are typical of magma-rich passive margins, and the margin has great potential for studying continental break-up and (magma-rich) passive margin formation.

## 1. Introduction

### 1.1. Geology of Afar

The Afar Depression in East Africa forms a triangular rift floor flanked by the Ethiopian Plateau in the west, the Somalian Plateau to the south and the Aisha and Danakil Blocks to the east and NE, respectively (Fig. 1a). Afar contains the triple junction between the Main Ethiopian Rift (MER), Gulf of Aden and Red Sea rift axes. At the Gulf of Zula in the north, the Red Sea axis steps into Afar and continues SE through the Danakil Depression and along the Dabbahu Manda-Harraro segments (McClusky et al., 2010). From the East, the Gulf of Aden axis enters Afar through the Gulf of Tajura, linking up with the Red Sea system in central Afar (Doubre et al., 2017). The MER, itself the northernmost segment of the East African Rift System, forms the third branch of the triple junction and interacts with the other branches at the Tendaho Goba'ad Discontinuity (Fig. 1a) (Pagli et al., 2019). The region is considered a key locality for the study of continental break-up processes, as it contains rift systems in various stages of development, from incipient rifting in the MER, ongoing breakup and passive margin formation in Afar proper, to active oceanic spreading occurs in the Red Sea and Gulf of Aden (e.g. Bosworth et al. 2005; Corti 2009, 2012; Zwaan et al. 2020a, and references therein).

The development of Afar started with the emplacement of one or multiple mantle plumes below East Africa from ca. 45 Ma (e.g. Ebinger & Sleep 1998; Rogers et al. 2000; Pik et al. 2006; Rooney et al. 2017), resulting in a massive outpouring of Trap series flood basalts over a 1 My time period around 30 Ma (Hoffmann et al. 1997) that covered large parts of the region (Mohr 1983a). Moreover, continental extension driven by the anticlockwise rotation of the Arabian plate initiated in the Gulf of Aden around 35 Ma and propagated towards Afar and subsequently the Red Sea basin at ca. 29 Ma and 23 Ma, respectively (Ukstins et al. 2002; Bosworth et al. 2005; Wolfenden et al. 2005, ArRejehi et al. 2010; Leroy et al. 2010; Szymanski et al. 2016; Purcell 2017, and references therein Fig. 1c). This rift configuration caused oblique extension along the WAM and other parts of the Red Sea-Gulf of Aden system (Smith 1993; Zwaan et al. 2020b, Fig. 1c). Around 11 Ma the Danakil Block, initially a part of the rift floor, began to independently rotate anticlockwise (McClusky et al. 2010), resulting in a local stress field change in Afar. Along the Western Afar Margin (WAM), this is thought to have resulted in NE directed extension changing to near orthogonal E-W extension (Zwaan et al. 2020b, Fig. 1d). The (northern) MER only formed around 11 Ma, long after the other two branches of the Afar triple junction were well established (Wolfenden et al. 2004).

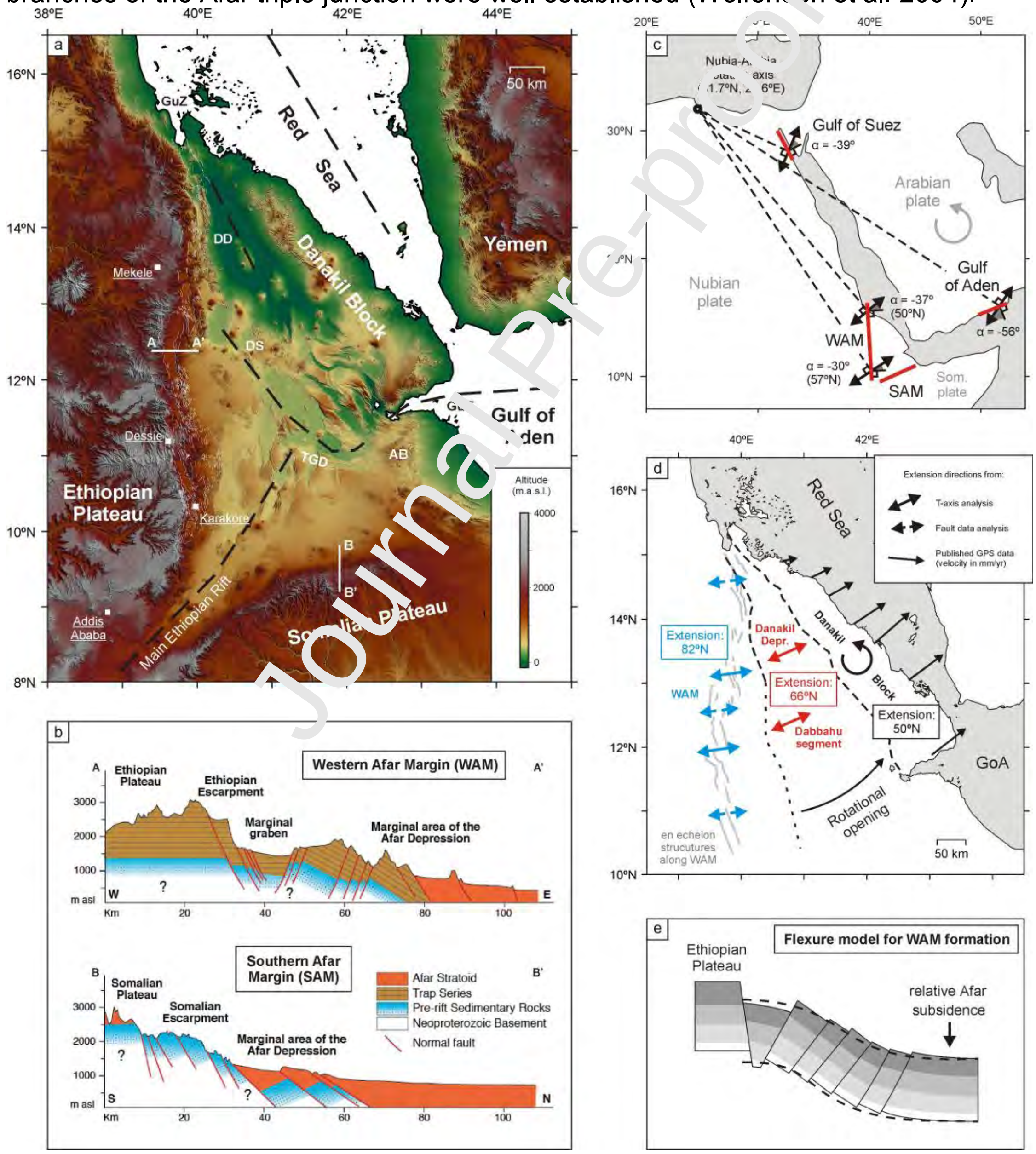


**Fig. 1.** Geology and tectonics of Afar and its western margin. (a) General map of Afar depicting the triple junction between the Red Sea, Gulf of Aden and Main Ethiopian Rift axes (dotted lines). AB: Aisha Block, DD: Danakil Depression, DS: Dabbahu Segment, GuT: Gulf of Tajura, GuZ: Gulf of Zula,

TGD: Tendaho-Goba'ad discontinuity. Topography is derived from ASTER GDEM data, which is a product of NASA and METI (Japan). (b) Structural sections of (top) the Western Afar Margin (WAM) and (bottom) the Southern Afar Margin (SAM). Antithetic faulting and the presence of a marginal graben characterize the former, whereas the latter is dominated by synthetic (basinward) faulting. Afar Stratoid: Pliocene-Pleistocene volcanics (e.g. Acocella 2010). Modified after Beyene & Abdelsalam (2005) and Corti et al. (2015a). (c) Relationship between the anticlockwise rotation of the Arabian plate and the extension directions along the Red Sea-Gulf of Aden system. The WAM should be undergoing sinistral oblique extension (angle α between -30˚ and -37˚), and did so during the first phase of WAM development, resulting in the right-stepping en echelon margin arrangement shown in (a) and (d). The SAM experienced highly oblique dextral extension. Modified after Smith (1993) ArRajehi et al. (2010) and Zwaan et al. (2020b). (d) Current tectonic setting in Afar, involving a rotational opening due to anticlockwise rotation of the Danakil Block about a pole at 17.0°N, 39.7°E. This tectonic situation diverges from the regional setting shown in (c), causing a near-orthogonal extension along the WAM since ca. 11 Ma. GoA: Gulf of Aden. Modified after McClusky et al. 2010, Zwaan et al. (2020b). (e) Concept of crustal flexure due to differential subsidence, explaining the distinct structural architecture of the WAM. Modified after Abbate & Sagri (1969).

### 1.2. The Western Afar Margin

The passive margins developing in Afar exhibit quite different structural architectures (Fig. 1b). The Southern Afar Margin (SAM) is dominated by synthetic (basinward) normal faulting and blocks rotated towards the Somalian Plateau (e.g. Black et al. 1972; Morton & Black 1975; Beyene & Abdelsalam 2005) (Fig. 1b). In contrast, The WAM is characterized by pervasive antithetic faulting, blocks and strata tilted towards Afar, and the presence of marginal grabens hugging the large escarpment faults (Fig. 1b) (e.g. Mohr 1962; Abbate et al. 1969; Mohr 1983b, Tesfaye & Ghebreab 2013; Corti et al. 2015a, Stab et al. 2016). The WAM, which forms the transition from the Ethiopian Plateau (altitudes over 3000 m) into the Afar Depression (partially below sea level), is the primary focus of this study.

The WAM marks important changes in crustal thickness and rheological properties. Active and passive seismic imaging of the plateau suggest that the crust is ~40 km thick (e.g. Hammond et al., 2011), with P wave velocity (Vp) and the ratio between P- and S-wave velocities (Vp/Vs) varying between that of typical to moderately intruded continental crust (Mackenzie et al., 2005; Hammond et al., 2011). The plateau's effective elastic thickness (Te) is high (55 km or more), suggesting most of the crust has elastic strength (Ebinger & Hayward, 1996). In contrast the crust is mostly ~20-25 km thick in Afar, decreasing to ca. 16 km in the north (Hammond et al., 2011; Lewi et al., 2016). Elevated Vp throughout the crust suggests that it is largely intruded with now solidified mafic intrusions. However, evidence for an increase in Vp/Vs ratio with increasing crustal depth from local seismicity and receiver functions (Keir et al., 2009; Hammond et al., 2011), coupled with high conductivity in the lower crust in magnetotelluric imagery (e.g. Desissa et al., 2013) also suggests current partial melt in the lower crust. This, coupled with a thin seismogenic crust and a Te of ~5 km in Afar (Ebinger & Hayward, 1996), infers that only the upper crust beneath Afar has elastic strength.

Various scenarios for the margin's structural evolution have been proposed, involving margin-scale block rotation accommodated by crustal creep, large-scale detachments, rollover structures and margin collapse, as well as crustal flexure (e.g. Chorowicz et al. 1999; Tesfaye & Ghebreab 2013; Stab et al. 2016). Zwaan et al. (2020a) reviewed these models and conclude that flexural deformation (e.g. Abbate & Sagri 1969, Fig. 1e) is the most probable mechanism, either induced by crustal-scale detachment faulting (Stab et al. 2016) or by differential loading due to continued magmatic intrusion of the Afar crust (Wolfenden et al. 2005, Corti et al. 2015b). Indeed, Afar has been highly volcanically active throughout its geological history (e.g. Acocella et al. 2010; Corti et al. 2015a; Stab et al. 2016), strongly weakening the lithosphere (e.g. Chang et al. 2011; Hansen & Nyblade 2013), and its margins can be considered to be on the magma-rich side of the passive margin spectrum (e.g. Rooney et al. 2013; Tugend et al. 2018 and references therein).

### 1.3. Aim of this study

Although various authors have described (parts of) the WAM (see review in Zwaan et al. 2020a and references therein), and Zwaan et al. (2020b) have recently provided an up-to-date description of the structural geology along the whole margin, the mechanisms underlying its formation remain poorly understood. Analogue and numerical modelling techniques are a reliable means to explore these questions. For instance Corti et al. (2015b) suggest that magmatic loading can generate large-scale crustal flexure, but these numerical models not reproduce the more detailed structural features of the margin.

Another potential mechanism for WAM-style margin formation is a (synthetic) basement fault, inducing flexure and marginal graben formation by deforming a brittle-viscous overburden as proposed in previous models (e.g. Naylor et al. 1994, Dooley et al. 2003, Hardy et al. 2018 and Gabrielsen et al. 2019). However these models simulate structures in the uppermost crust (i.e. deformation above an evaporite layer) and are difficult to scale up, especially since there is little evidence for a similar (lithospheric-scale) fault below the WAM (e.g. Hammond et al. 2011; Zwaan et al. 2020a). Furthermore, Livio et al. (2019) provide a method to test flexure of brittle layers, but only focus on the uppermost crust. Furthermore, flexure is applied symmetrically (i.e. doming), which is different from the situation along the WAM (Fig. Fig. 1b, e). Finally, Zwaan et al. (2019) apply rapid extension and a velocity discontinuity, inducing lower crustal stretching and upper crustal flexure. Yet, the resulting rift is symmetric, with flexure on both sides, whereas Afar is strictly asymmetrical since flexure does not occur along the Danakil block or Yemen margin. Previous works are thus not directly applicable to the WAM because they focus on much smaller-scale systems, do not properly reproduce the tectonic setting, or do not provide sufficient insights into the detailed structural development of the margin.

In this study we therefore test factors that may lead to the development of a WAM-style passive margin by means of centrifuge experiments. We run a first series of models exploring the effects of brittle crust thickness, rheological contrasts between the rift and its shoulder as well as syn-tectonic sedimentary loading in orthogonal extension. A subsequent set of experiments aims to reproduce the tectonic setting during the first and second phases of WAM development, including en echelon margin structures and oblique extension. We subsequently compare our results with previously published modelling work, the WAM itself and established magma-rich passive margins.

## 2.2. Methods

### 2.2.1. Centrifuge modelling

Applying a centrifuge for analogue modelling allows the manipulation of model gravity and the use of different (viscous) materials from those in normal-gravity analogue experiments of lithospheric deformation (e.g. Corti et al. 2003, 2004; Agostini et al. 2011, Corti, 2012; Philippon et al. 2015; Fig. 2a, b). The relatively stiff viscous materials applied in enhanced-gravity models make model handling and preparation easier than in the case of normal-gravity experiments (Ramberg 1981, Schellart, 2002; Corti et al. 2003). When using a centrifuge, both the model and an equal counterweight are placed within the apparatus. During a model run, both the model and the counterweight start rotating with high velocity around the central axis, while their containers adapt to the increasing centrifugal forces. These forces translate to an enhanced gravity (18 *g*) in the model, thus deforming the model materials (see section 2.2.4 and Appendix A2), by means of gravitational collapse, rather than externally applied extension.

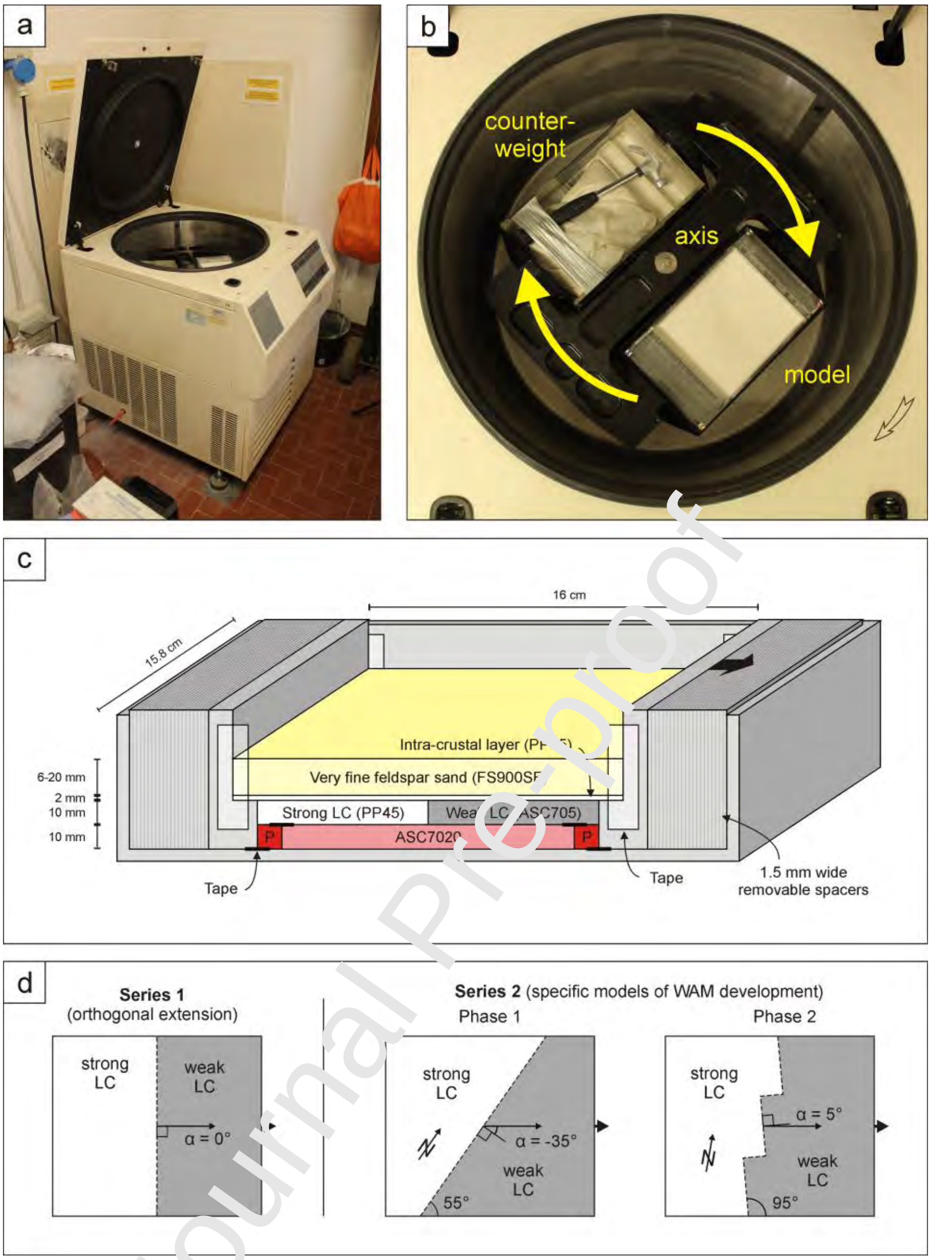


**Fig. 2.** Centrifuge apparatus and model set-up. (a) Centrifuge in the Tectonic Modelling Laboratory of CNR-IGG at the Earth Sciences Department of the University of Florence. (b) Interior of the centrifuge during a model run. The machine contains an inner construction with two pods that can rotate about a vertical axis. The model is placed in one pod, and a counterweight in the other. The model is deformed by rapidly rotating the inner part, generating centrifugal forces that simulate enhanced gravity. During rotation, the pods, which are also suspended by horizontal hinges, tilt into a vertical position so that the centrifugal forces act vertically on the model surface. (c) 3D depiction of the general model set-up. The model materials are contained between two sets of removable spacers and two L-shaped blocks. The weak viscous ASC7020 bottom layer allows free deformation of the overlying materials. The relatively strong viscous PP45 and weak viscous SCA705 represent the stronger and weaker lower crust (LC) below the Ethiopian Plateau and Afar, respectively. An optional thin layer of PP45 on top serves to reduce the rheological contrast between the two domains. Finally, a layer of very fine feldspar sand (FS900SF) represents the brittle upper crust. In order to impose asymmetric extension on the model, one of the spacers is removed and the model put into the centrifuge (b), where the enhanced gravity induces gravitational collapse to fill in the space left by the spacer. Tape is used at various locations to prevent boundary effect. (d) Map view geometries of the rheological contrast. Left: model set-up for orthogonal extension and general parameter testing (series 1 models). Middle and right: specific set-ups to mimic the tectonic situation during the first and second phases of WAM development (series 2 models).

### 2.2.2. Model design

Models are contained within a plexiglass box with 25 cm x 15.8 cm inner dimensions (Fig. 2c). At both far ends plexiglass spacers and L-shaped blocks are placed, the latter with a 2 cm high base, leaving a 14 cm x 15.8 cm space at the model base (Fig. 2c). Here, a 1 cm thick bottom layer consisting of a very weak viscous mixture (SCA7020) is placed, flanked by 1 cm bars of sturdy plasticine (Giotto Pongo). The next 1 cm thick stratum contains two domains, both 7 cm long, the first consisting of a relatively strong viscous material (PP45) and the second of a relatively weak viscous mixture (SCA705). These two domains represent the stable and weak lower crust below the Ethiopian Plateau and Afar, respectively (Fig. 1a), and are covered by a ca. 2 mm sheet of the same PP45 mixture that extends onto the L-shaped blocks. This thin intra-crustal level serves to reduce the rheological contrast between both domains. Finally, a cover of feldspar sand (FS900SF) represents the brittle upper crust in the Afar region (Fig. 2c). A cm in our models translates to ca. 15 km in nature. For detailed material properties, see Appendix A1.

During a model run, we step-by-step remove the 1.5 mm thick spacers on the right-hand side to allow space for the model to deform asymmetrically, as we only simulate one margin of the Afar rift system (Fig 2c). The centrifuge applies 18 *g* to the model, thus forcing the model material into the space left open by the spacer. The lower layer, which does not directly correspond to a lithospheric layer, allows deformation of the crustal analogues: the weak lower crust is expected to stretch and collapse, whereas its resistant counterpart remains stable. As a result, the overlying layers warp downward into "Afar", creating a crustal flexure (Fig. 1e).

By applying scaling laws (e.g. Hubbert 1937; Ramberg 1981; Weijermars & Schmeling 1986) we demonstrate that our models are well suited for simulating the Afar crust (detailed scaling calculations are presented in Appendix A2). Specifically, the models have a geometric scaling ratio of $6.7 \cdot 10^{-7}$, such that 1 cm correspond to 15 km in nature. The extension velocities in our models (ca. $2.5 \cdot 10^{-5}$ m/s) translate to ca. 10 mm/y in nature, close to velocities found in the Afar region (i.e. between 5 and 20 mm/y, e.g. McClusky et al. 2010; Saria et al. 2014). Also dimensionless scaling ratios are very similar between model and nature, so that scaling requirements are fulfilled (Appendix A2).

**2.2.3. Model parameters**

A total of 14 experiments testing the influence of various parameters on crustal flexure and margin development in orthogonal extension are completed (series 1), of which an overview is presented in table 1. In these, the brittle cover thickness is varied (from 0.6 to 2.0 cm). Furthermore, the effect of an enhanced rheological contrast is studied by removing the thin intra-crustal level in selected experiments. We furthermore include sedimentation to test the effects of loading (somewhat similar to the magmatic loading mechanism proposed by Wolfenden et al. 2005). This is simulated by filling in the model topography to the pre-deformed level with the same FS900SF feldspar sand used for the brittle cover after every second time-step (i.e. $t_2$ or 3.0 mm, $t_4$ or 6.0 mm and $t_6$ or 9.0 mm extension, respectively). Every sedimentation step is marked by a thin (<1 mm) layer of dyed sand for analysis of vertical displacements in final cross-sections. Similar thin layers are also added to the sand layer representing the upper crust. The total extension in our series 1 models amounts to 10.5 mm (ca. 15 km) over 7 intervals.

An additional set of oblique extension models serves to directly simulate the different phases of WAM development (series 2, Fig. 2d, table 1). Two models involve a -35˚ oblique extension (i.e. angle α, measured between the normal to the rheological contrast and the extension direction, Fig. 2d, middle), which reflects the tectonic setting during the initial phase of WAM development (Fig. 1c, Smith 1993; Zwaan et al. 2020b). A further experiment involves 5˚ oblique extension with respect to a right-stepping rheological contrast, which represents the en echelon structural arrangement of the WAM resulting from the first tectonic phase (Fig. 2e, right, Zwaan et al. 2020b). These en echelon structures were reactivated under near-orthogonal extension due to more recent Danakil Block rotation (Fig. 1d, Zwaan et al. 2020b). Our series 2 models contain a thin intra-crustal layer, but no sedimentation is applied. Total extension deviates from the series 1 models: 15 mm and 12 mm, respectively (Table 1).

**Table 1. Model parameters**

| | Model | PP45 intra-crustal layer | Sand thickness | Sedimentation | Details | Shown in: |
|---|---|---|---|---|---|---|
| Series 1 | A | X | 6 mm | - | | Figs. 3-6 |
| | *$A_2$* | *X* | *6 mm* | | *Rerun of A* | Figs. 3, 4, 6 |
| | B | X | 10 mm | - | | Figs. 3, 4, 6 |
| | C | X | 15 mm | - | | Figs. 3-6 |
| | *$C_2$* | *X* | *15 mm* | - | *Rerun of C* | |
| | *$C_3$* | *X* | *15 mm* | - | *Rerun of C* | |
| | *$C_4$* | *X* | *15 mm* | | *Rerun of C* | |
| | D | X | 20 mm | - | | Figs. 3, 4, 6 |
| | E | X | 6 mm | X | | Figs. 3, 4, 6 |
| | F | X | 15 mm | X | | Figs. 3, 4, 6 |
| | G | - | 6 mm | - | | Figs. 3-6 |
| | H | - | 15 mm | - | | Figs. 3-6 |
| | I | - | 6 mm | X | | Figs. 3, 4, 6 |
| | J | - | 15 mm | X | | Figs. 3, 4, 6 |
| Series 2 | K | X | 15 mm | - | 35˚ oblique extension | Fig. 8 |
| | *$K_2$* | *X* | *15 mm* | - | *35˚ oblique extension, rerun of K* | |
| | L | X | 15 mm | - | 5˚ oblique extension + steps | Fig. 8 |

### 2.2.4. Model analysis

We apply various methods to analyze internal and external model evolution. Top- and side view photographs taken after completion of each deformation interval provide a first-order record of model evolution. Furthermore, pictures taken from various angles serve to reconstruct model topography over time through photogrammetry software (Agisoft Photoscan). The resulting digital elevation models (DEMs) are further processed using Global Mapper and QGIS software for a detailed and quantified assessment of model topography development. Finally, after model completion, the sand layers are soaked, frozen and cut to obtain cross-sections. Thin levels of dyed sand in both the cover layer and the sedimentary infill subsequently reveal (syn-sedimentary) internal deformation.

## 3. Results of series 1 models

### 3.1. Final structures

An overview of final model surface structures from series 1 is presented in Fig. 3. There is a clear distinction between models with and without syn-rift sedimentation, as the former have a flatter topography due to the repeated infilling of the rift basins. A further overview of final cross-sections is provided in Fig. 4, showing that the weak lower crust collapses in all models, leading to deformation and faulting in the brittle cover above the rheological contrast between the strong and weak lower crustal analogues..

Distinct structural differences are associated with the increasing brittle layer thickness in models A-D (with intra-crustal layer, without sedimentation, Figs. 3a-d, 4a-d). Whereas model A (0.6 cm thick brittle cover) develops very limited normal faulting as the brittle layer is warped, model B and C (1.0 and 1.5 cm brittle cover, respectively) produce marginal graben structures (Figs 3a-c, 4a-c). The associated antithetic normal fault in model B is not readily visible on the cross-section (Fig. 4b), possibly due to a very small throw or the soaking of the sand before freezing and cutting, but is clearly present on the top view photograph (Fig. 3b) and in the case of model C also visible in section (Fig. 4c). Model C furthermore contains a larger antithetic fault more basinward (Fig. 4c). Increasing the brittle layer thickness to 2.0 cm leads to the formation of a second graben structure downslope. Note that the flexural domain in models A-D is dominated by large synthetic faults, whereas (visible) antithetic faulting is constrained to the marginal graben boundary faults (Figs. 3b-c, 4b-c).

Models G and H (without intra-crustal layer or sedimentation, and a 0.6 and 1.5 cm sand cover, respectively, Figs. 3g, h, 4g, h) fit the trend described above; the former develops a minor marginal graben similar to that of model B, while the latter contains a wider fault zone reminiscent of the structures in model D, although no clear antithetic faulting is involved (Figs. 3b, d, g, h, 4b, d, g, h). The structures in Models G and H are generally more developed in comparison to their direct equivalents with the same brittle cover thickness, but with an intra-crustal layer (Models A and C, Figs. 3a, c, g, h, 4a, c, g, h).
The models with sedimentation (models E, F, I and J, Figs. 3e, f, i, j, 4 e, f, i, j), form the same general features as their counterparts without sedimentation, except that the accommodation space created in the latter is almost fully filled with sediments. The only important difference is that the models with sedimentation develop a slightly higher total subsidence and synthetic fault offset is increased (see section 3.3).

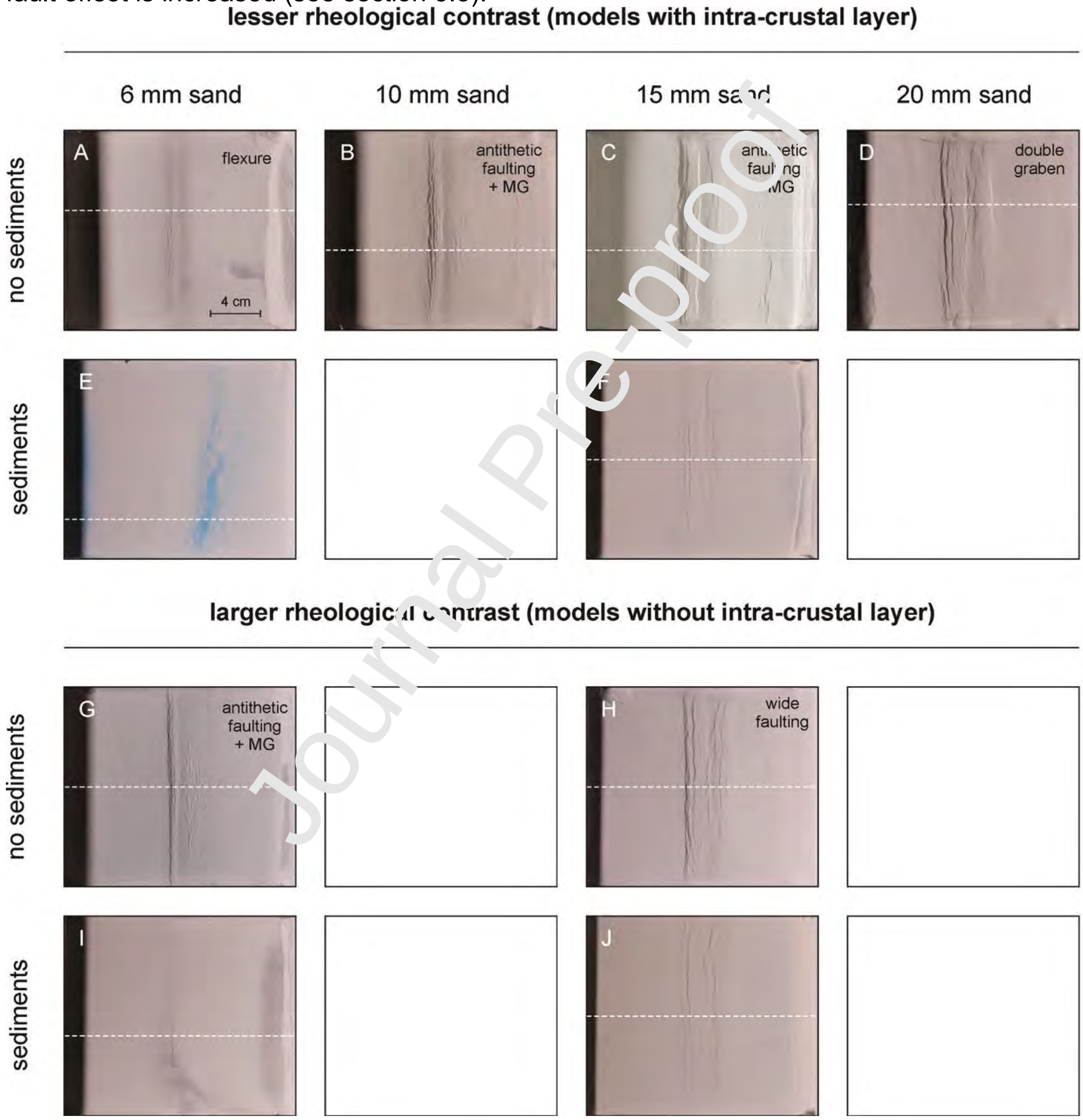


**Fig. 3.** Map view summary of final reference model structures as a function of brittle layer thickness, the presence of a thin intra-crustal layer and sedimentation. Lighting from the left. MG: marginal graben.

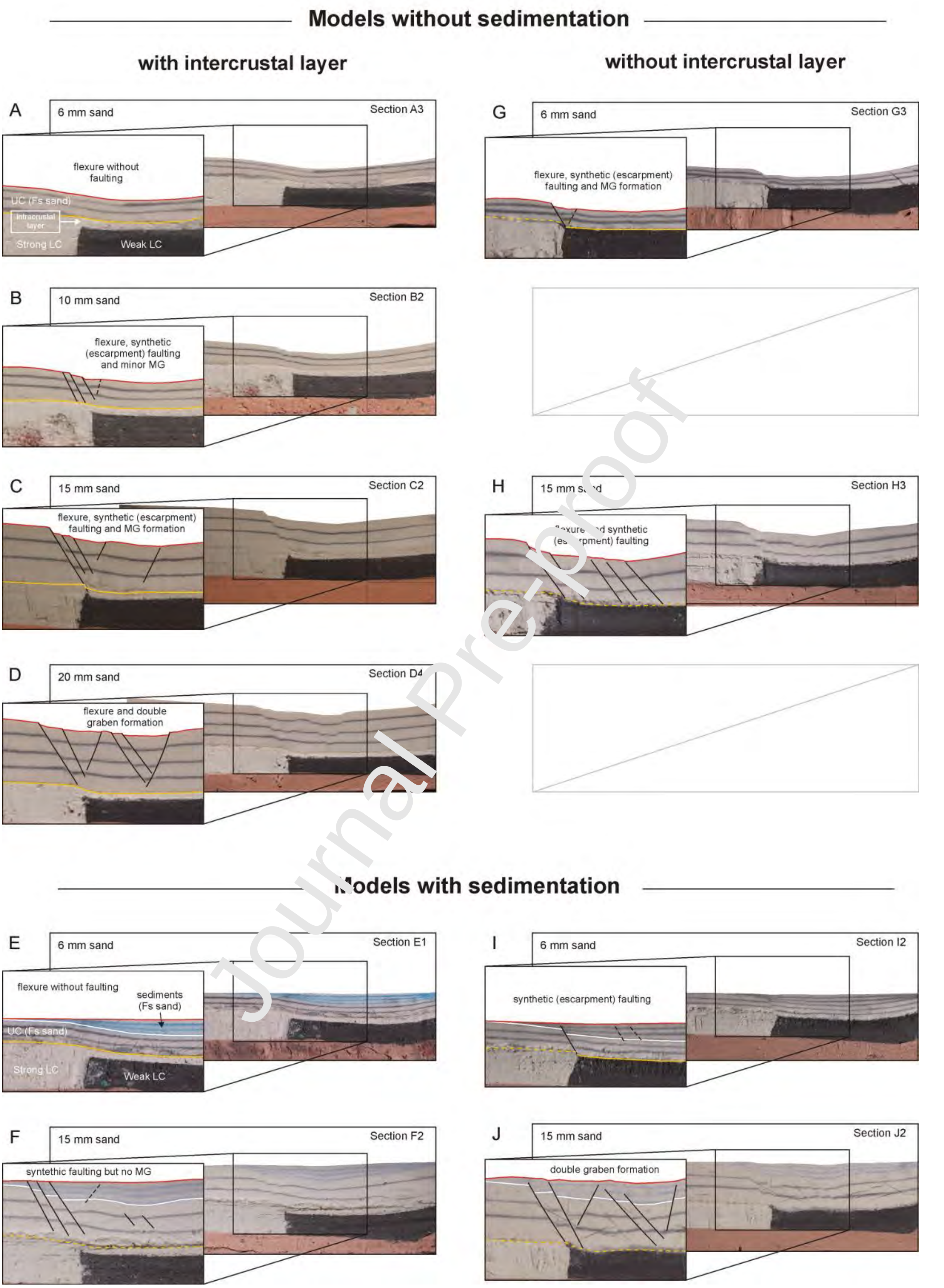


**Fig. 4.** Cross-section summary of final reference model structures as a function of brittle layer thickness, the presence of a thin intra-crustal layer and sedimentation. Insets show our structural interpretation. The strong and weak lower crustal analogues are light grey and black, respectively. LC: lower crust, MG: marginal graben. Section locations are shown in Fig. 3.

## 3.2. Structural evolution in map view

The final top views and cross sections illustrate that models without intra-crustal layer form more developed structures than their counterparts containing such a layer (Figs. 3, 4). These differences in structural maturity are highlighted when analyzing the surface evolution of selected experiments without sedimentation (models A, C, G and H, the former two with, and the latter two without intra-crustal layer, respectively, Fig. 5). In all these models, some surface deformation is apparent after 1.5 mm of extension. Faulting appears after 3.0 mm of extension ($t_2$) in model C, whereas model A does not develop any clear faults at all (Fig. 5a, b). By contrast, models G and H, without intra-crustal layer, develop distinct faulting early on (between 1.5 and 3.0 mm of extension [t1-2], Fig. 5c, d). Furthermore, initial faulting is synthetic, forming an escarpment fault system between rift shoulder and rift floor, eventually followed by (in most cases) antithetic faulting and marginal graben formation (Figs. 3-5). Only models A and H differ, as the former develops pure flexure, whereas the latter is dominated by the main escarpment fault system and synthetic faulting (Fig. 4a, h).

### 3.3. Topographic analysis

Photogrammetry-derived DEMs allow a detailed analysis of model topography and subsidence, best shown in cumulative subsidence graphs along the central axis of the experiments (Fig. 6). For models without sedimentation, these are equivalent to their topography. In the case of models with sedimentation, topography remains rather flat over time (Fig. 3) and the cumulative subsidence values are obtained by summing up the topographic difference between sedimentation intervals instead.

Most subsidence plots are very similar, in that they are dominated by an (synthetic) escarpment fault, established during the initial phases of deformation (i.e. $t_{1-3}$, Fig. 6), accommodates a large amount of the model's vertical displacement due to the downwarping of the margin. Only Model A does not develop such a dominant fault, instead it shows a gradual flexure towards the basin (Fig. 6a). In contrast, the marginal grabens, if present, only appear during the final stages of model development ($t_{5-7}$, Fig. 6).

Furthermore, the maximum subsidence in all series 1 experiments shows a clear positive correlation between the thickness of the brittle cover and the subsidence (Fig. 7a). We also observe that models without an intra-crustal layer of PP45 (i.e. with a more pronounced contrast between both lower crustal domains) as well as models with sedimentation tend to have higher degrees of maximum subsidence (Fig. 7b-e).


**Fig. 5.** Comparing surface evolution of selected series 1 models with and without intra-crustal layer. All models are without syn-rift sedimentation.

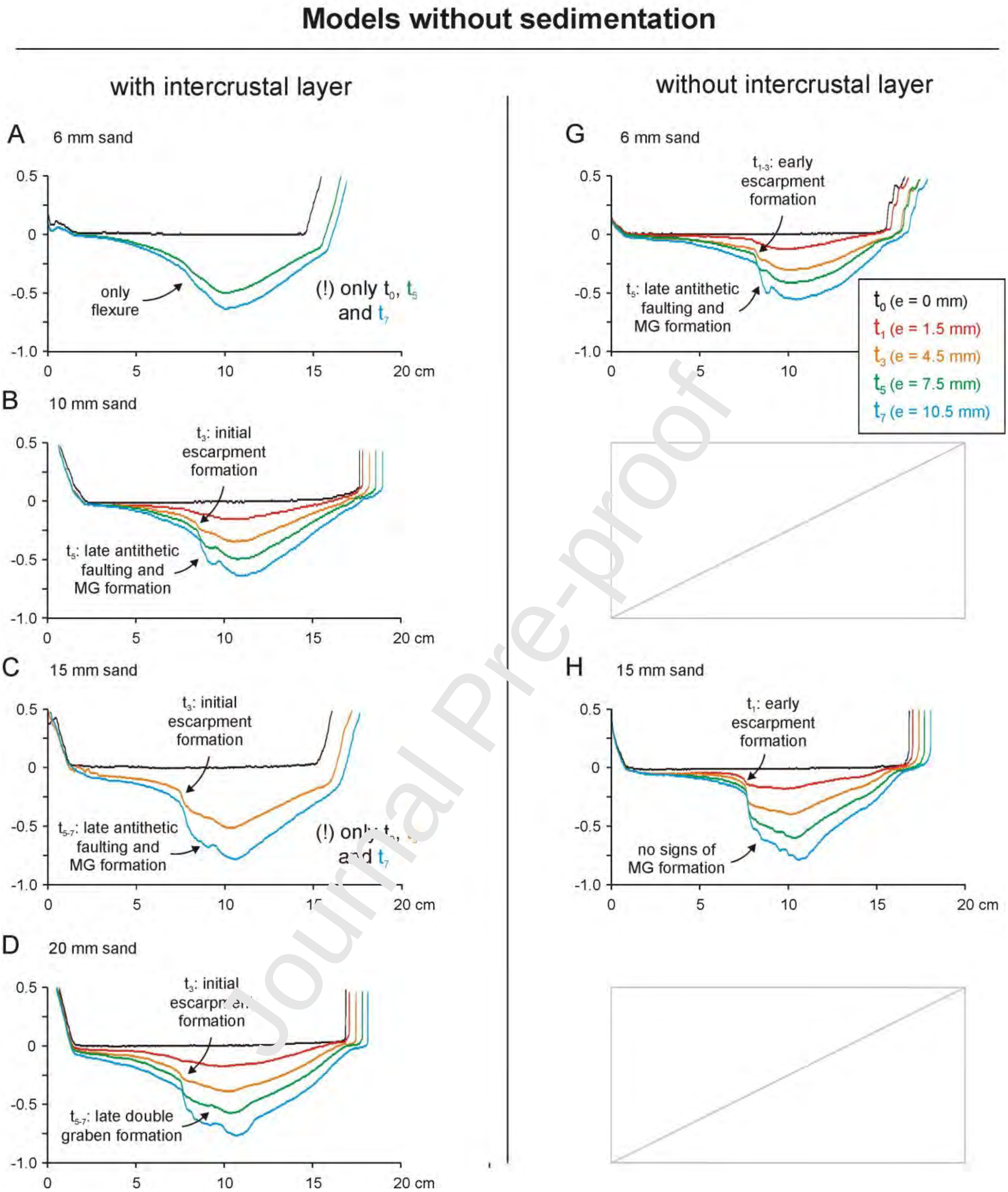


**Fig. 6.** Subsidence evolution overview of selected experiments from series 1 (Models A-D, G and H, without sedimentation). The graphs, showing cumulative subsidence along a profile through the center of the experiments, are derived from DEMs obtained via photogrammetry techniques. Time steps shown: $t_0$, $t_1$, $t_3$, $t_5$ and $t_7$ (i.e. 0, 1.5, 4.5, 7.5 and 10.5 mm or extension, see legend in model G). Note that some time steps are missing in Models A and C. MG: marginal graben.

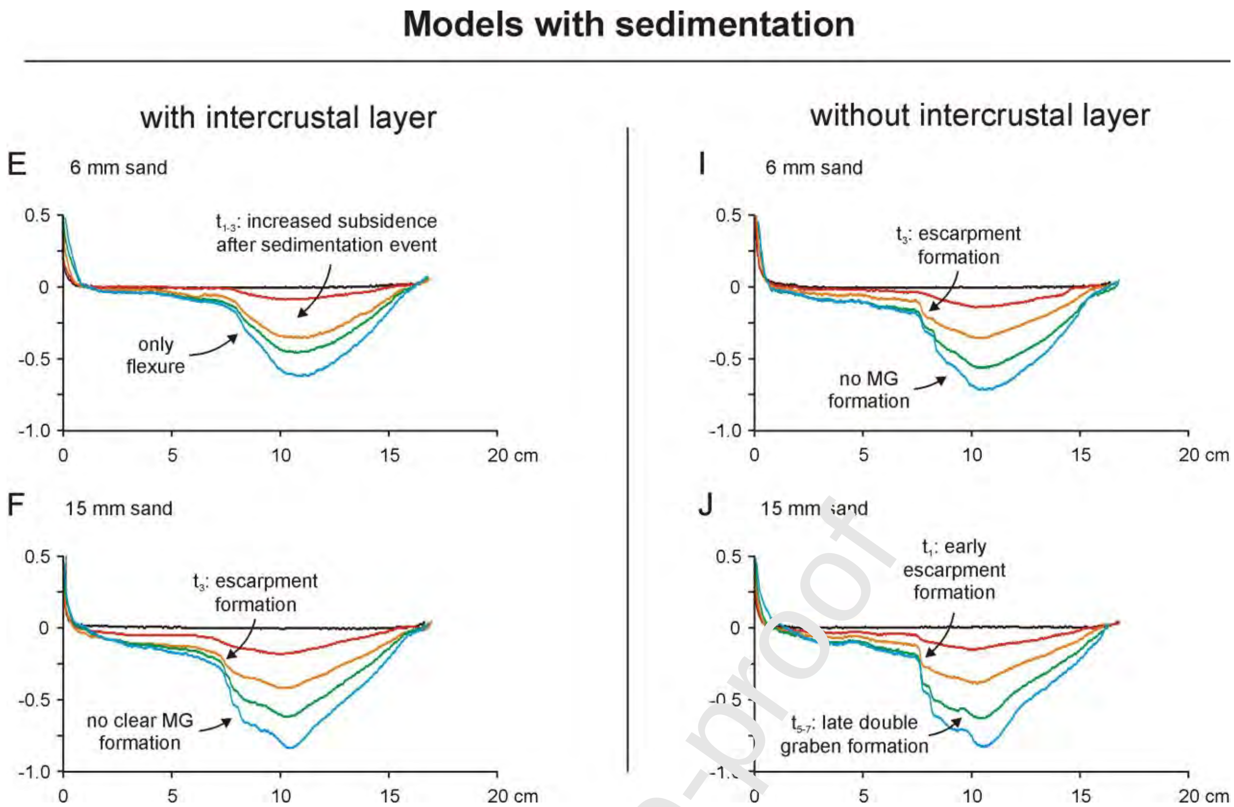


**Fig. 6 (continued).** Subsidence evolution overview of selected experiments from series 1 (Models E, F, I and J, with sedimentation). The graphs, showing cumulative subsidence along a profile through the center of the experiments, are derived from DEMs obtained via photogrammetry techniques. Time steps shown: $t_0$, $t_1$, $t_3$, $t_5$ and $t_7$ (i.e. 0, 1.5, 4.5, 7.5 and 10.5 mm or extension, see legend in model G). MG: marginal graben.

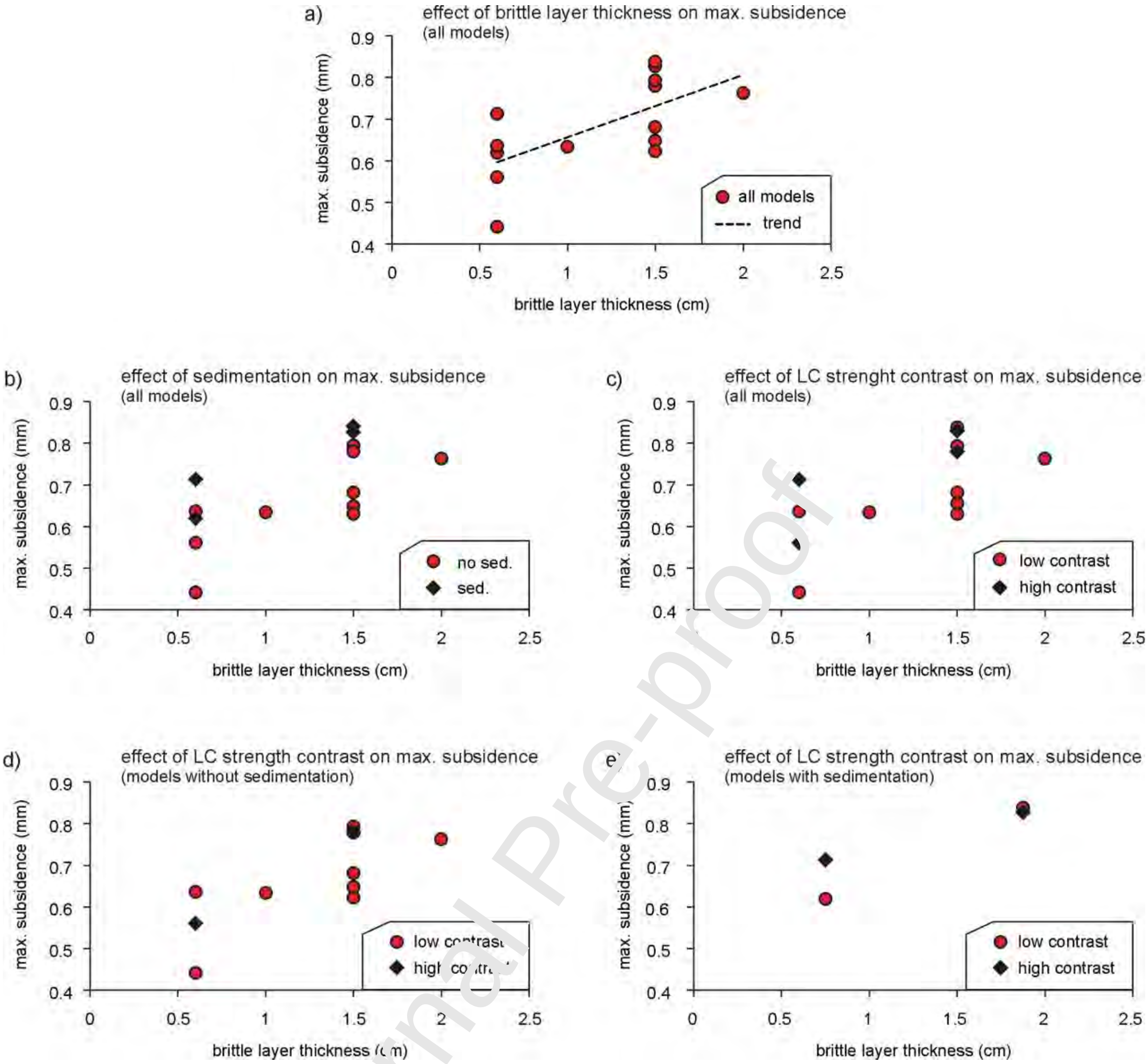


**Fig. 7.** Maximum subsidence plots measured on topographic profiles from our series 1 models (Fig. 6). LC: lower crust.

### 3.4. Results from series 2 models

Next to the orthogonal extension series 1 models, we run a set of models to more specifically represent the two phases of WAM evolution (Series 2, Figs. 1c, d, 8). For these models, the layering of model C is adopted (i.e. an intra-crustal layer and a 1.5 cm thick the sand cover). Total applied extension is slightly higher than in the series 1 experiments (15 and 12 mm for models K and L, respectively, Fig. 8b, g).

Model K reproduces the first phase of WAM development involves 35˚ sinistral oblique extension with respect to the inferred N-S striking lower crustal rheological contrast along the margin (Figs. 1c, 2d, 8a). This model develops a series of right-stepping en echelon normal faults (Fig. 8a-e), which are dominantly synthetic and develop largely sub-perpendicular to the general extension direction, Their en echelon arrangement allows the general escarpment to follow the rheological contrast. The lack of antithetic faulting leads to the absence of marginal grabens along the escarpment (Fig. 8a-e), although some faulting deviates from this trend where the rheological contrast is farthest away from the moving sidewall (around Section K1).

Model L simulates the second phase of WAM evolution and involves a right-stepping rheological contrast mimicking the right-stepping character of the margin, inherited from the first phase of oblique extension simulated in Model K (Figs. 1a, 2d, 8). Extension is slightly oblique (5˚ with respect to the direction of the right-stepping segments and 10˚ to the general N-S orientation of the WAM (Figs. 1d, 8). The rheological contrast focuses deformation and flexure, developing a distinct right-stepping en echelon series of escarpment faults and marginal grabens (Fig. 8f-j).

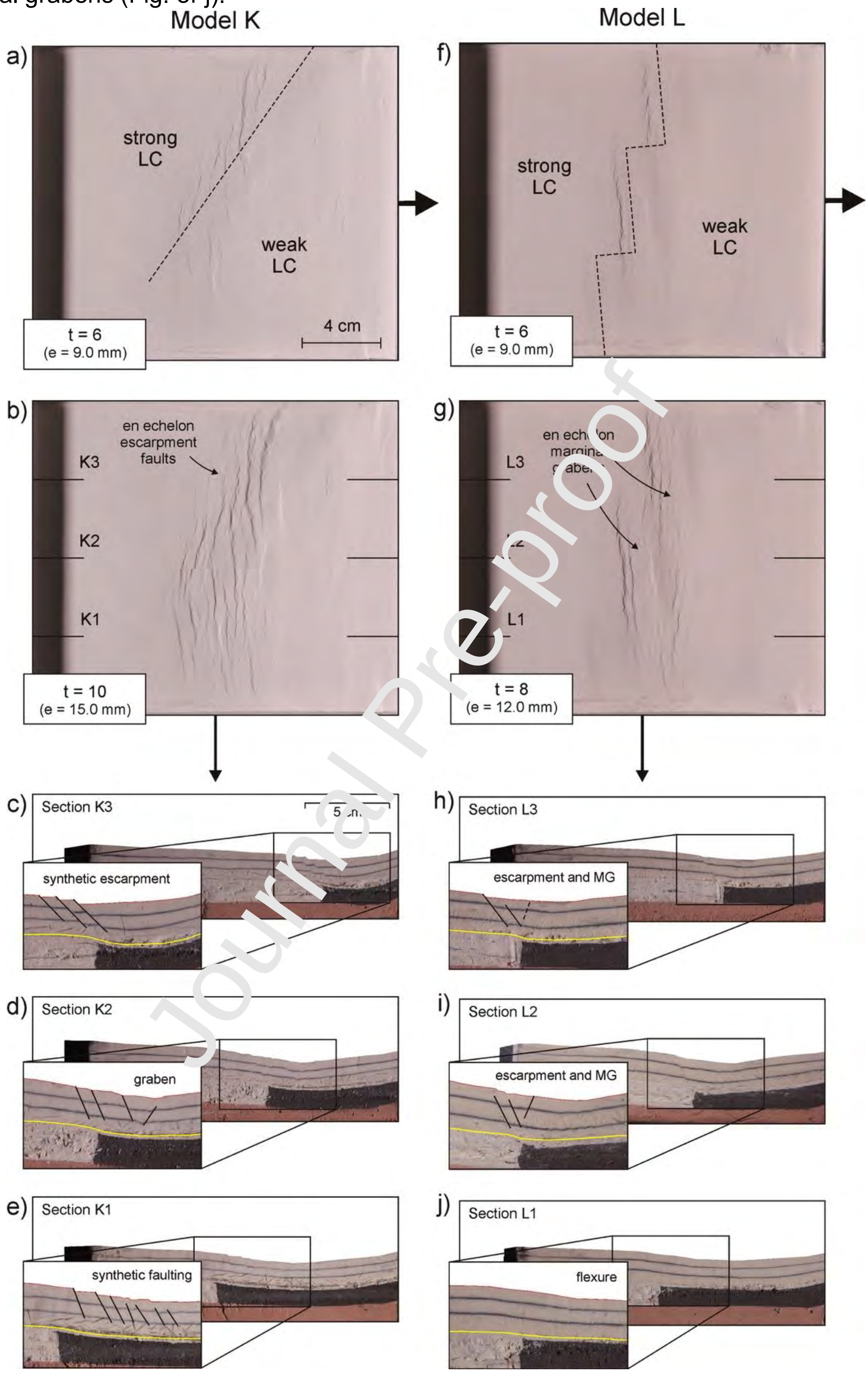


**Fig. 8.** Surface evolution and cross-sections of models K and L, aiming to simulate the tectonic setting along the Western Afar Margin during its first and second development phase, respectively (Fig. 1c, d). In section view, the strong and weak lower crustal analogues are light grey and black, respectively. Dotted lines indicate the transition form a strong LC (lower crust) to a weak lower crust analogue. MG: marginal graben.

## 4. Discussion

### 4.1. Synopsis of model results

Our models, of which an overview is presented in Fig. 9, illustrate how the stretching of a locally weaker ductile lower crust leads to rift margin development. Generally we observe flexure of the overlying brittle layer that deforms as a factor of its thickness and the rheological contrast between the lower crust below the plateau and the rift floor (Fig. 9a). Pure flexure occurs with a thin brittle layer and a moderate rheological contrast; due to the relatively low brittle strength flexure can be accommodated by small-scale deformation, rather than by large faults (Figs. 3a, 4a, e, 5, 6a, e, 9a). In contrast, a large change in the lower crustal strength causes strong localization of deformation above the rheological transition and the development of large synthetic faults to accommodate subsidence (Figs. 3, 4g, h, i, j, 5, 9a).

The larger structures observed with increasing brittle cover thickness are due to the increased strength of the brittle layer preventing marginal flexure from being accommodated via small-scale internal deformation only (Fig. 9a). Therefore, flexure leads to escarpment development, antithetic faulting and even (double) marginal graben formation, when the lower crustal rheological contrast is moderate (Figs. 3d, 4d, j, 5, 9a). For higher strength contrasts, the enhanced localization of deformation forces the development of synthetic faults (Figs. 4g, i, 5, 9a).

The models containing marginal grabens follow a distinct evolution (Fig. 9b). Initially, differential subsidence leads to marginal flexure without clear faulting at the surface: minor deformation can still be accommodated internally (Figs. 5, 6, 8b, $t_1$). The first clear faults are synthetic and occur along the developing escarpment (Figs. 5, 6, 8b, $t_2$). Continued flexure forces the development of antithetic faulting and marginal grabens that represent the "keystone" in the flexural arch, as explained by the Abbate & Sagri (1969) structural model (Figs. 1e, 9b, $t_3$). Based on this concept and supported by field data (Figs. 1b, e), we should also expect the development of pervasive antithetic faulting in our models. Such structures likely have too small an offset to discern on our model scale. This is highlighted by the smaller (antithetic) normal faults observed in model map views, which are often not readily visible in section (Figs. 3, 4, 8).

The addition of syn-rift sedimentation does not significantly alter large-scale model features. The associated enhanced subsidence must be due to increased loading above the weak lower crustal analogue (Figs. 7, 9c, Zwaan et al. 2018). This loading effect also explains why maximum subsidence intensifies with increasing sand cover thicknesses (Fig. 7b). This effect is enhanced by a higher rheological contrast, which allows for easier fault development and rapid localized subsidence, rather than more widespread flexure (Fig. 7c-e). Furthermore, the increased throw along the main faults when sedimentation occurs is described in previous modelling studies (e.g., Corti et al., 2010; Poliakov et al. 2014; Zwaan et al. 2018).

Finally, our experiments suggest that extension direction has an important impact on margin development. Marginal grabens are typical of (near) orthogonal extension systems (Figs. 3-7, 8e-l, 9d), whereas oblique extension leads to the creation of en echelon synthetic faults (Figs. 8a-e, 9d). These results are in agreement with analogue models by Agostini et al. (2011) and Corti et al. (2013), which also develop marginal graben-like structures, but only when (local) extension conditions are near-orthogonal. We conclude that orthogonal extension provides the best conditions for margin "collapse" as it would create maximum space. By contrast, in oblique extension systems the margin is stabilized by the hanging wall block, which moves partially along the margin, rather than 90˚ away from it (Fig. 9d) (Chorowicz et al. 1999).

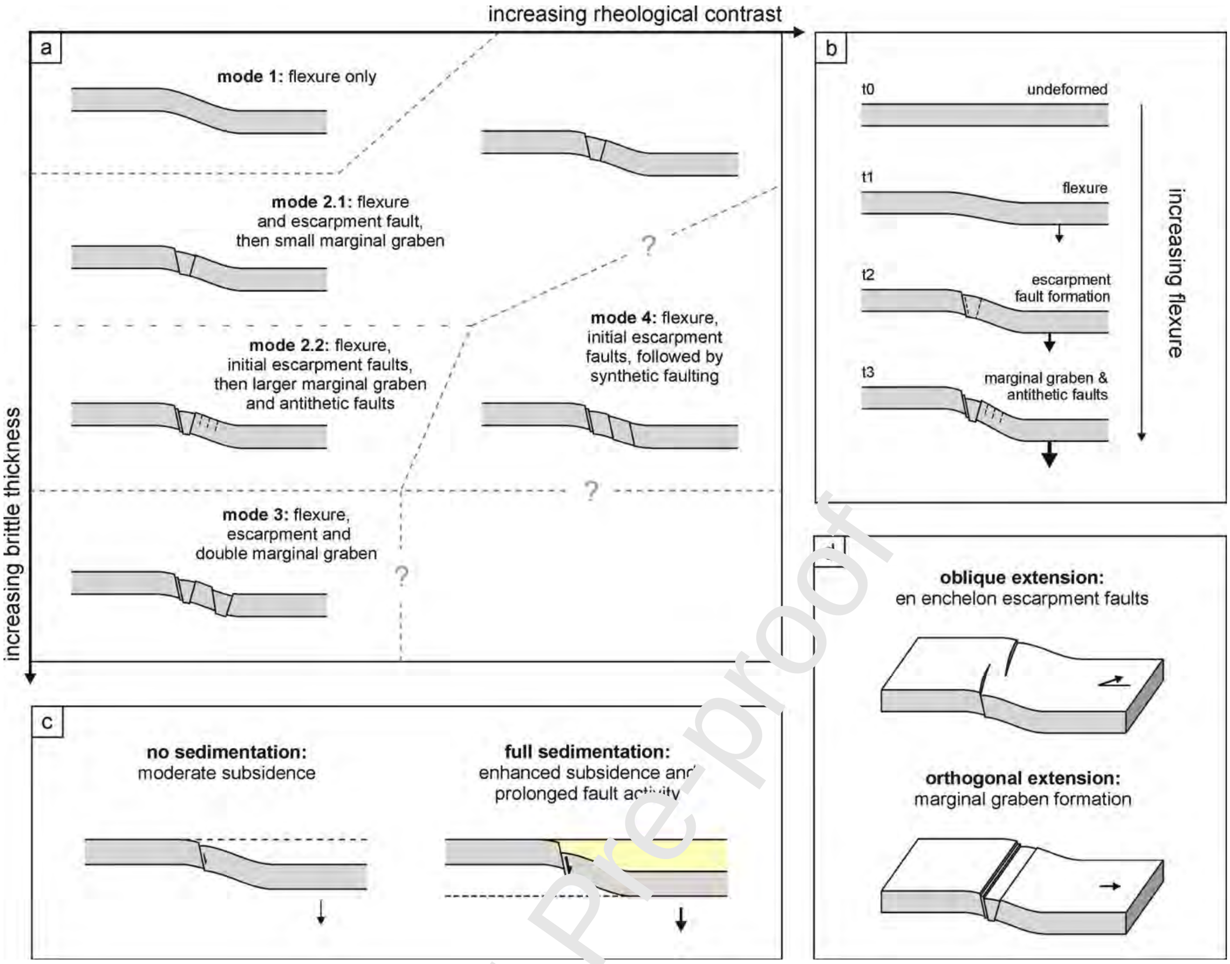


**Fig. 9.** Summary of model results. (a) Relationships between the different modes of margin development and (1) brittle layer thickness, as well as (2) rheological contrast. Both a thicker brittle layer and a stronger rheological contrast promote the development of faults and (marginal) grabens, of which mode 2.2 is very similar to the structure of the Western Afar Margin (WAM) (Fig. 1b). Note that the gradient from mode 1 (pure flexure) to mode 3 (double graben) is in a sense also a gradient in deformation intensity. (b) Sequence of developments during marginal flexure: initial flexure (t1) is followed by synthetic escarpment development (t2) and finally clear antithetic faulting and marginal graben development. (c) Contrast between models with and without syntectonic sedimentation; syn-rift sedimentation leads to continued deformation along large faults, and the loading due to the extra material causes increased subsidence. (d) Effects of extension direction on margin style. Oblique extension causes en echelon escarpment faulting, whereas orthogonal extension allows marginal grabens to develop.

### 4.2. Implications for the evolution of the Western Afar Margin

When comparing our models with the WAM, the orthogonal extension models with a 1.5 cm brittle layer and moderate rheological contrast present a good fit (Figs. 1a, b, 3c, 4c). The brittle cover thickness scales up to ca. 30 km, which is consistent with the maximum depth of earthquakes along the WAM (Illsley-Kemp et al. 2018, Zwaan et al., 2020b). Furthermore the early escarpment fault development, followed by late antithetic faulting and marginal graben initiation (Fig. 8b) is in agreement with the eroded nature of the WAM escarpment, which must have accommodated large amounts of deformation at an early stage, but seems currently relatively inactive (Tesfaye & Ghebreab 2013; Illsley-Kemp et al. 2018; Zwaan et al. 2020b, Fig. 1a, b). In contrast, the relatively fresh and active fault scarps of the antithetic faults, and the thin sedimentary infill of the marginal grabens (< 500 m, often much less) along the WAM, suggests these features are relatively young (Abbate et al. 2015; Illsley-Kemp et al. 2018; Zwaan et al. 2020b). This interpretation is also supported by geochronological analysis on volcanic rocks found along the WAM (Wolfenden et al. 2005; Rooney et al. 2013).

However, a comprehensive interpretation must include the multiphase evolution of Afar. We therefore present a tectonic reconstruction, somewhat similar to a scenario proposed by

Chorowicz et al. (1999), involving the different rift phases and their impact on the WAM (Fig. 10). Initially, the rotation of the Arabian plate causes sinistral oblique extension along the WAM (Smith 1993; Zwaan et al. 2020b), leading to the development of the large-scale, right-stepping en echelon escarpment faults reproduced in model K (Figs. 8a-e, 9d, 10). Subsequently, the shift in extension direction from sinistral oblique to near-orthogonal due to the individualization of the Danakil Block around 11 Ma (McClusky et al. 2010; Zwaan et al. 2020b) allows enhanced flexure. This causes antithetic faulting, as well as marginal graben development along the previously established escarpment arrangement as simulated in model L (Figs. 8f-j, 9b, d, 10).

Our model results fit well with the features observed along the WAM, yet there is some potential discrepancy. Afar has been highly magmatically active for most of its geological history (e.g. Rooney et al. 2013; Stab et al. 2016 and references therein). These processes may not only have weakened the Afar lithosphere as simulated in our models, but may have locally added mass through intrusion of mafic material, causing (additional) subsidence and flexure (Wolfenden et al. 2005, Corti et al. 2015b, Fig 11a). Instead, we induce flexure by differential stretching of the lower crust rather than by a localized (magmatic) loading. Nevertheless, our results remain valid; even if magma loading would be the driving force of flexure along the WAM, the effects on the deforming brittle crust and the associated surface expression should be similar to those in our models.

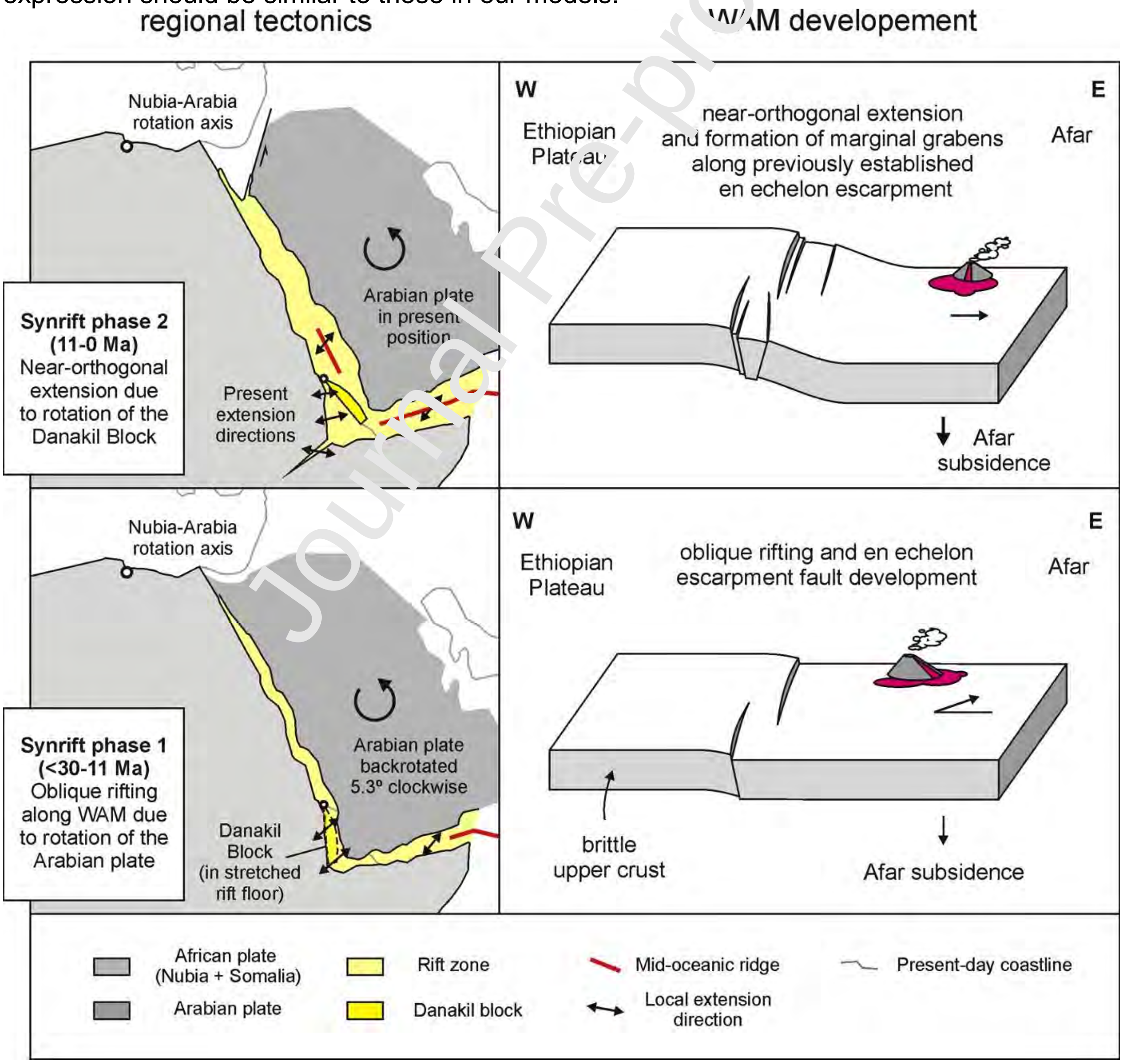


**Fig. 10.** Evolution of the Western Afar Margin within its regional context as derived from our model results. The first syn-rift phase involves sinistral oblique extension due to the counterclockwise rotation

of the Arabian plate, leading to the development of an en echelon style escarpment, as seen in model K. The second phase of rifting involves near-orthogonal extension due to the independent rotation of the Danakil block, leading to flexure and the development of marginal grabens as observed in model L. Note that magmatism has remained active during the development of Afar. Modified after Bosworth et al. (2005), Bosworth (2015), Zwaan et al. (2020b).

### 4.3. Implications for continental rifting and passive margin development

The WAM displays antithetic faulting, basinward tilted blocks, as well as the overlying lava flows that dip towards the basin (Fig. 1b), similar to the characteristic seaward dipping reflectors (SDRs) observed on seismic sections (Fig. 11a) of magma-rich passive margins (e.g. those offshore Norway and in the south Atlantic. Buck 2017; Paton et al. 2017; Norcliffe et al. 2018, Tugend et al. 2018, Fig. 11b). Along the margin of Uruguay, there is also evidence for the presence of marginal grabens (Fig. 11b).

The point that marginal grabens, such a distinct topographical feature along the WAM, seem to be so rare globally may have various reasons. Firstly, the marginal graben structures are rather small compared to the rift basin as a whole. Instead, the margin is dominated by the escarpment, with the marginal grabens only accommodating a minor amount of deformation and sedimentary infill (Fig 1c, Abbate et al. 2015; Zwaan et al. 2020b), which is mirrored in our model sections and subsidence profiles (Figs. 4, 6). As such, any marginal grabens may be too insignificant to stand out on margin-scale seismic lines. Furthermore, our models suggest that a significant amount of flexure is necessary to create marginal grabens (Fig. 9b), and the differential vertical motion between the >3 km high Ethiopian Plateau and Afar, partially below sea level, may be rare. Finally, our models suggest that marginal graben formation is favored by near-orthogonal extension (Fig. 9d). In nature, rifting most commonly has an oblique component (e.g. Brune 2016), thus hampering the development of marginal grabens. Perhaps this explains why the SAM, which has undergone highly oblique extension due to its orientation with respect to the Arabian plate (Fig. 1a, c), has not developed large-scale flexure and marginal grabens (Fig 1b). Yet at its western end, the SAM is more aligned with the MER and extension is rather orthogonal (Sani et al. 2014; Fig. 1a, c, 10). Here, the margin has undergone some flexure as well (Tesfaye et al. 2003). Further south along the MER, more cases of marginal flexure occur (e.g. Wolfenden et al. 2004; Corti et al. 2018). This highlights that even though rifting is often considered to result in normal faulting and graben development, flexure may under certain circumstances replace the classic fault-bounded rift architecture.

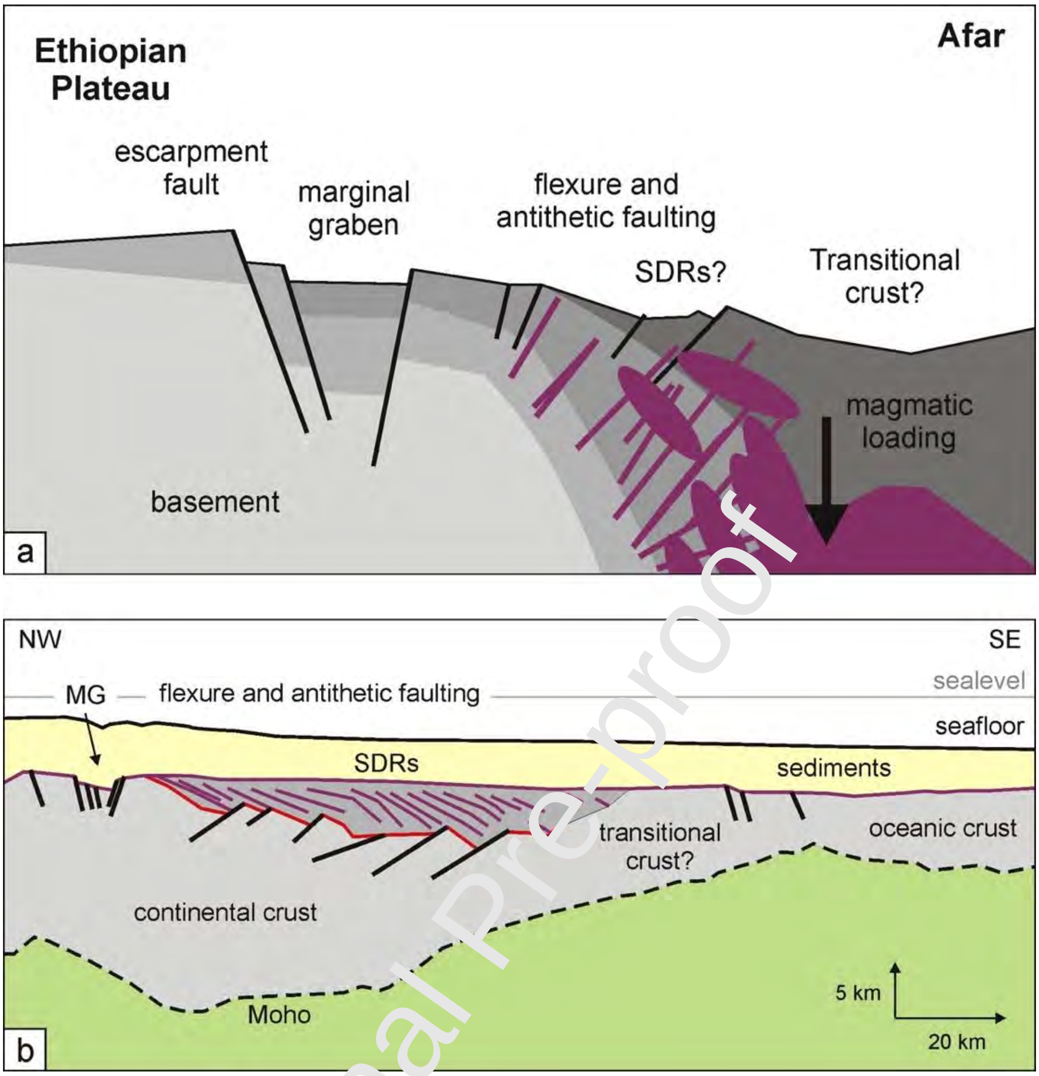


**Fig. 11.** Magmatic loading mechanism and relation with magma-rich passive margins. (a) Section of the WAM, showing the typical marginal grabens and antithetic faulting, as a result of magmatic loading. Note the volcanic layers that may form the equivalent of seaward-dipping reflectors (SDR) on seismic lines. Modified after Wolfenden et al. (2005) and Corti et al. (2015b). (b) Interpreted seismic section offshore Uruguay, showing a potential marginal graben (MG), SDRs above antithetic faults. Note the similarity with the transitional crust in (a). Modified after Tugend et al. (2018).

## 5. Conclusions

Our analogue modelling efforts exploring the development of WAM-type rift margins through crustal flexure lead us to the following conclusions:

- We find that marginal flexure can occur due to the differential extension of a weak lower crustal domain, potentially enhanced by magmatic loading, and the concept of marginal flexure can elegantly explain the structural features observed along the WAM.
- The thickness of the brittle crust controls the type of structures marginal flexure causes. A thinner brittle crust can easily accommodate flexure, leading to a gentle basinward flexure. In contrast, increasing layer thicknesses lead to faulting, mainly of large synthetic escarpment faults. Flexural deformation of thicker layers also create antithetic faulting and marginal grabens. A thicker brittle crust also causes more subsidence due to increased loading.
- A stronger contrast between the competent and weak lower crust due to the absence of an intra-crustal layer causes more localized deformation and enhances subsidence along the resulting synthetic faults.

- Most deformation is accommodated by large synthetic escarpment faults that develop early on. Antithetic faulting and marginal grabens are late and relatively minor features within a rift margin that undergoes flexure.
- Basin-wide sedimentation leads to more loading and enhanced subsidence, as well as longer activity along large (escarpment) faults. These effects are however different from those predicted by the magmatic loading model (Wolfenden et al. 2005), probably because the latter type of loading is much more localized along the rift axis.
- Oblique extension leads to the development of en echelon synthetic escarpment faults, but prevents the occurrence antithetic faulting and marginal grabens, the latter can only form in near-orthogonal extension conditions.
- Our results support a scenario in which the early evolution of the WAM was characterized by oblique extension and en echelon synthetic escarpment fault development, due to the orientation of the WAM and the direction of Arabian plate motion. Only after the Danakil Block started rotating independently, near-orthogonal extension conditions were established, allowing enhanced flexure, antithetic faulting and marginal graben formation along the previously created en echelon escarpment.
- The influence of oblique extension explains why the WAM and SAM have such different structural characteristics, and why marginal grabens are not often observed in nature. The other characteristics of the WAM (flexure, antithetic faulting, potential SDRs) are typical of magma-rich passive margins. The WAM has thus great potential for improving our understanding of the processes involved in continental break-up and (magma-rich) passive margin formation.

**Data availability**

Rheological measurements of the brittle and viscous materials applied in our models are available in the form of two open access data publications via GFZ Data Services (Zwaan et al. 2020c and 2020d, respectively). A third open access data publication available via GFZ Data Services (Zwaan et al. 2020e) contains additional images, digital elevation data and videos of our experiments. Links to these datasets are provided in the references.

**Acknowledgements**

We kindly thank Daniele Maestrelli for his support in the tectonic laboratory and introducing us to Photoscan, as well as Kirsten Elger and Matthias Rosenau for helping us publish our supplementary material in the form of three GFZ Data Publications (Zwaan et al. 2020c-e). Constructive feedback by Sandy Cruden and an anonymous reviewer are greatly appreciated. This project was funded by the Swiss National Science Foundation (Early Postdoc Mobility grant P2BEP2_178523 (http://p3.snf.ch/project-178523) awarded to FZ, and by PRIN2017 grant 2017P9AT72.

**Appendix A. Material properties and scaling.**

**A1. Detailed material description**

We use various brittle and viscous experimental materials (table A1). The upper crust and syn-rift sediments are simulated with fine, angular Feldspar sand type FS900SF from Amberger Kaolinwerke. This sand has a grainsize of 20-100 μm with a significant fine fraction (50% <30 μm) and a density of ca. 1000 kg/m$^3$ when poured from ca. 10 cm height (Montanari et al. 2017). Ring-shear tests (Zwaan et al. 2020c) yield a cohesion of 121 Pa and an internal friction angle of 35.7˚, a dynamic friction angle of 33.8˚ and a reactivation friction angle of 35.7˚. The internal friction angle differs from those empirically measurement by Montanari et al. (2017), who report a value of ca. 57˚.

A mixture of PDMS (SGM-36 Polydimethylsiloxane produced by Dow Corning) and Pongo (plasticine putty produced by FILA [FILA 2020]) represents the strong domain of the lower crust. This PP45 mixture (100 g PDMS mixed with 45 g Pongo) has a density of 1520 kg/m$^3$. The power law exponent (n-number) is 4.8 for our model strain rates of ca. $2{\cdot}10^{-4}$/s (see details on viscous rheologies in Zwaan et al. 2020d). The intra-crustal layer in selected models is also made of PP45. The weak lower crust consists of Dow Corning 3179 putty mixed with fine corundum sand and oleic acid following a 100:70:05 weight ratio. This SCA705 mixture has a density of 1660 kg/m$^3$ and an n-number of 6.7 (details in Zwaan et al. 2020d).

The lowermost model layer, which allows deformation of the overlying layers consists of the same components as the SCA705 mixture, but in a different ratio. Instead of a 100:70:05 ratio between Dow Corning putty, corundum sand and oleic acid, we apply a 100:70:20 ratio. The resulting SCA7020 mixture has a density of 1610 kg/m$^3$, and a power law exponent of 9.1 (details in Zwaan et al. 2020d).

These values are valid for modelling temperature (20˚C). When temperatures increase, the viscous materials generally become less viscous (Zwaan et al. 2020d). Therefore, the centrifuge apparatus has an internal temperature control system allowing constant modelling conditions.

Table A1. Material properties

| **Brittle material** | | |
|---|---|---|
| FS900SF very fine feldspar sand[a, b] | Grain size | 20–100 $\mu$m (90% of total grains) |
| | Density (poured) | ca. 1000 kg/m$^3$ |
| | Peak internal friction angle | 35.7˚ |
| | Dynamic friction angle | 33.8˚ |
| | Reactivation friction angle | 35.7˚ |
| | Cohesion (peak) | 121 ± 13 Pa |
| **Viscous materials** | | |
| PP45 | Components (weight ratio) | Dow Corning SGM-36 PDMS[c] (100) and Giotto Pongo[d] (45) |
| | Density | 1520 kg/m$^3$ |
| | Viscosity[e] | $1.0 \cdot 10^7$ Pa·s |
| | Power law number (n)[f] | 4.8 |
| SCA705 | Components (weight ratio) | Dow Corning 3179 putty[g] (100), fine corundum sand (70), oleic acid (05) |
| | Density | 1660 kg/m$^3$ |
| | Viscosity[e] | $4.6 \cdot 10^5$ Pa·s |
| | Power law number (n)[f] | 6.7 |
| SCA7020 | Components (weight ratio) | Dow Corning 3179 putty[g] (100), fine corundum sand (70), oleic acid (20) |
| | Density | 1610 kg/m$^3$ |
| | Viscosity[e] | $4.2 \cdot 10^5$ Pa·s |
| | Power law number (n)[f] | 9.1 |

a) FS900SF is a product of Amberger Kaolinwerke (http://www.quarzwerke.com/)
b) Data from Montanari et al. (2017) and Zwaan et al. (2020c).
c) SGM-36 Polydimethylsiloxane (PDMS) formerly produced by Dow Corning, now part of Dow Chemical (www.dow.com)
d) Giotto Pongo (plasticine): produced by FILA (https://www.fila.it/it/en/product/giotto-pongo)
e) The viscosity of the materials varies with strain rate (shear thinning behavior). The listed viscosities are only valid for our model strain rates of ca. $2 \cdot 10^{-4}$/s. See Zwaan et al. (2020d) for more details.
f) The rheology of the viscous materials, although generally shear-thinning, is divided in a fast and slow regime, with $10^{-2}$/s as a threshold value. Here the n-number associated with our model strain rates of ca. $2 \cdot 10^{-4}$/s are given (see Zwaan et al. 2020d for more details)
g) 3179 putty formerly produced by Dow Corning, now part of Dow Chemical (www.dow.com)

**A2. Model scaling**

The crust is represented by a brittle and viscous layers. The brittle layer thickness ranges between 0.6 and 2 cm, whereas the viscous layer is always 1 cm thick. Following the discussion by Zwaan et al. (2019), we consider the models with a brittle-to-thickness ratio of 1.5 (i.e. 1.5 cm sand cover) as the most realistic and use this as a base for our scaling calculation.

Geometric scaling in the models is $6.7 \cdot 10^{-7}$, such that 1 cm in the models correspond to 15 km in nature (ratio convention: model/nature). The stress ratio between model and nature ($\sigma^*$) is obtained via the following equation (Hubbert 1937; Ramberg 1981): $\sigma^* = \rho^* \cdot h^* \cdot g^*$. Here $\rho^*$, $h^*$ and $g^*$ represent the density, length and gravity ratios respectively, and the equation yields a $\sigma^*$ of ca. $7 \cdot 10^{-6}$.
Dynamic similarity in the brittle layers can be validated using the the Rs ratio (Ramberg 1981; Mulugeta 1998; Bonini et al. 2001): Rs = gravitational stress/cohesive strenght = $(\rho \cdot g \cdot h) / C$, where $\rho$ is the density, g the gravitational acceleration, h the height and C cohesion. The calculations yield Rs values of 22 and 15 for the model and nature, respectively, which is very similar ensuring dynamic scaling of the brittle behavior. Moreover, the internal friction angle of the sand, is very similar that of upper crustal rocks (e.g. Byerlee 1978, Table A2).
For the scaling of viscous materials, the stress ratio $\sigma^*$ and viscosity ratio $\eta^*$ produce the strain rate ratio $\dot{\varepsilon}^*$ with the subsequent formula: $\dot{\varepsilon}^* = \sigma^*/\eta^*$ (Weijermars & Schmeling 1986) and subsequently, the velocity ratio v* and time ratios t* through the following equations: $\dot{\varepsilon}^* = v^*/h^* = 1/t^*$.
Given that every time step represents 1.5 mm of extension over a steady state 18 *g* interval of ca. 1.5 min (i.e. an extension velocity of $2.5 \cdot 10^{-5}$ m/s*) and an initial model width of 14 cm (Fig. 2c), strain rates in our models are in the order of $1 \cdot 10^{-4}$/s*. For the strong lower crust analogue (PP45), this value translates to a viscosity of ca. $1.0 \cdot 10^{7}$ Pa·s (Zwaan et al. 2020d, Table A1). Combined with an estimated viscosity of $1 \cdot 10^{23}$ Pa·s for the strong lower crust in nature, our model deformation corresponds to an extension velocity of ca. 10 mm/y, which is close to values observed in Afar and the MER (i.e. between 5 and 20 mm/y, e.g. McClusky et al. 2010; Saria et al. 2014).
To test dynamic similarity of the viscous layers, we apply the Ramberg number $R_m$ (Weijermars & Schmeling 1986): $R_m = (\rho \cdot g \cdot h^2) / (\eta \cdot v)$. This number is 0.17 in both our models and nature for the strong lower crust (Table A2). For the weak lower crust the $R_m$ values are 0.44 and 0.43, respectively. Together with the Rs values the Ramberg numbers indicate that scaling requirements are reasonably fulfilled.
**FOOTNOTE:** * Due to the design of the apparatus, no direct observation of model deformation during a centrifuge run can be made hence the reported values are estimations. However, the results of several previous papers, and the successful comparison with many natural examples have shown that effects such as the short acceleration and deceleration phases during an experimental run have a negligible influence on centrifuge modeling results (e.g. Corti et al. 2003; Corti 2012).

**Table A2. Scaling parameters**

| | | Model | Nature (Afar) |
|---|---|---|---|
| **General parameters** | Gravitational acceleration (g) | 177 m/s$^2$ | 9.81 m/s$^2$ |
| | Extension velocity (v) | ca. $2.5 \cdot 10^{-5}$ m/s (60 mm/h) | ca. $3.5 \cdot 10^{-10}$ m/s (10 mm/y) |
| **Brittle layer** | Material/represents | FS900SF feldspar sand | Upper crust/sediments |
| | Thickness (h)* | $1.5 \cdot 10^{-2}$ | $2.4 \cdot 10^{4}$ |
| | Density (ρ) | ca. 1000 kg/m$^3$ | 2700 kg/m$^3$ |
| | Internal friction angle | ca. 36° | ca. 31° |
| | Cohesion (C) | 121 ±13 Pa | $40 \cdot 10^{6}$ Pa |
| **Strong viscous layer** | Material/represents | PP45 | Strong lower crust |
| | Thickness (h) | $1 \cdot 10^{-2}$ m | $1.6 \cdot 10^{4}$ m |
| | Density (ρ) | 1610 kg/m$^3$ | 2900 kg/m$^3$ |
| | Viscosity (η)** | $1.0 \cdot 10^{7}$ Pa·s | $1 \cdot 10^{23}$ Pa·s |
| **Weak viscous layer** | Material/represents | SCA705 | Weak lower crust |
| | Thickness (h) | $4 \cdot 10^{-2}$ m | $1.6 \cdot 10^{4}$ m |
| | Density (ρ) | 1660 kg/m$^3$ | 2950 kg/m$^3$ |

| | | | |
|---|---|---|---|
| | Viscosity (η)** | $4.0\cdot10^{6}$ Pa·s | $4\cdot10^{22}$ Pa·s |
| **Weak viscous bottom layer** | Material/represents | SCA720 | - |
| | Thickness (h) | $1\cdot10^{-2}$ m | - |
| | Density (ρ) | 1610 kg/m$^{3}$ | - |
| | Viscosity (η)** | $4.2\cdot10^{5}$ Pa·s | - |
| **Dynamic scaling values** | Brittle stress ratio ($R_s$) | 22 | 15 |
| | Ramberg number ($R_m$)*** | 0.17 and 0.44 | 0.17 and 0.43 |

***** a 1.5 cm thick sand cover over a 1 cm thick viscous layer is taken as the most realistic thickness ratio for continental crust (see e.g. Zwaan et al. 2019).
****** model viscosities valid for model strain rates ($\dot{\varepsilon}$) of ca. $2\cdot10^{-4}$/s
*** $R_m$ given for the strong lower crust and weaker crust, respectively

**References**

Abbate, E., Sagri, M. 1969. Dati e considerazioni sul margine orientale dell'altiplano etiopico nelle province del Tigrai e del Wollo. Bollettino della Società Geologica Italiana 88, 489–497.
Abbate, E., Bruni, P., Sagri, M. 2015. Geology of Ethiopia: A Review and Geomorphological Perspectives. In: Billi, P. (ed) Landscapes and Landforms of Ethiopia, World Geomorphological Landscapes. Springer Science+Business Media, Dordrecht, 33-64. doi:10.1007/978-94-017-8026-1_2
Acocella, V., 2020. Coupling volcanism and tectonics along divergent plate boundaries: collapsed rifts from Central Afar, Ethiopia. GSA Bulletin 132 , 1717-1728.
Agostini, A., Bonini, M., Corti, G., Sani, F., Mazzarini, F. 2011. Fault architecture in the Main Ethiopian Rift and comparison with experimental models: Implications for rift evolution and Nubia–Somalia kinematics. Earth and Planetary Science Letters 301, 479-492. doi:10.1016/j.epsl.2010.11.024
ArRajehi, A., McClusky, S., Reilinger, R., Daoud, M., Alchalbi, A., Egintav, S., Gomez, F., Sholan, J., Bou-Rabee, F., Ogubazghi, G., Haileab, B., Fisseha, S., Asfaw, L., Mahmoud, S., Rayan, A., Bendik. R., Kogan, L. 2010. Geodetic constraints on present - day motion of the Arabian Plate: Implications for Red Sea and Gulf of Aden rifting. Tectonics 29, TC3011. doi:10.1029/2009TC002482
Beyene, A., Abdelsalam, M.G. 2005. Tectonics of the Afar Depression: A review and synthesis. Journal of African Earth Sciences 41, 41-59. doi:10.1016/j.jafrearsci.2005.03.003
Black, R., Morton, W.H., Varet, J. 1972. New Data on Afar Tectonics. Nature Physical Science 240, 170–173. http://dx.doi.org/10.1038/physci240170a0
Bonini, M., Sokoutis, D., Mulugeta, G., Boccaletti, M., Corti. G., Innocenti, F., Manetti, P., Mazzarini, F. 2001. Dynamics of magma emplacement in centrifuge models of continental extension with implications for flank volcanism. Tectonics 20, 1053– 1065. doi:10.1029/2001TC900017
Bosworth. W., Huchon P., McClay, K. 2005. The Red Sea and Gulf of Aden Basins. Journal of African Earth Sciences 43, 334-378. doi:10.1016/j.jafrearsci.2005.07.020
Bosworth, W. 2015. Geological Evolution of the Red Sea: Historical Background, Review, and Synthesis. In: Rasul N., Stewart I. (eds) The Red Sea. Springer Earth System Sciences. Springer, Berlin, Heidelberg. doi:10.1007/978-3-662-45201-1_3
Brune, S., Williams, S.E., Müller, D. Oblique rifting: the rule, not the exception. Solid Earth 9, 1187-1206. doi:10.5194/se-9-1187-2018
Buck, W.R. 2017. The role of magmatic loads and rift jumps in generating seaward dipping reflectors on volcanic rifted margins. Earth and Planetary Science Letters 466, 62–69. http://dx.doi.org/10.1016/j.epsl.2017.02.041

Byerlee, J.D. 1978. Friction of Rocks. Pure and Applied Geophysics 116, 615–626. doi:10.1007/BF00876528
Chang, S-J., Merino, M., Van der Lee, S., Stein, S., Stein, C.A. 2011. Mantle flow beneath Arabia offset from the opening Red Sea. Geophysical Research Letters 38, L04301. doi:10.1029/2010GL045852
Chorowicz, J., Collet, B., Bonavia, F., Korme, T., 1999. Left-lateral strike-slip tectonics and gravity induced individualisation of wide continental blocks in the western Afar margin. Eclogae Geologicae Helvetiae, 92, 149-158.
doi:10.5169/seals-168656
Corti, G., Bonini, B., Conticelli, S., Innocenti, F., Manetti P., Sokoutis, D. 2003. Analogue modelling of continental extension: a review focused on the relations between the patterns of deformation and the presence of magma. Earth-Science Reviews 63, 169-247.
doi:10.1016/S0012-8252(03)00035-7
Corti, G., Bonini, M., Sokoutis, D., Innocenti, F., Manetti, P., Cloetingh, S., Mulugeta, G. 2004. Continental rift architecture and patterns of magma migration: A dynamic analysis based on centrifuge models. Tectonics 23, TC2012.
doi:10.1029/2003TC001561
Corti, G. 2009. Continental rift evolution: From rift initiation to incipient break-up in the Main Ethiopian Rift, East Africa. Earth-Science Reviews 96, 1-53.
doi:10.1016/j.earscirev.2009.06.005
Corti, G. 2012. Evolution and characteristics of continental rifting: Analog modeling-inspired view and comparison with examples from the East African Rift System. Tectonophysics 522-523, 1-33.
doi:10.1016/j.tecto.2011.06.010
Corti, G., Ranalli, G., Mulugeta, G., Agostini, A., Sani, F., Zugu, A. 2010. Control of the rheological structure of the lithosphere on the inward migration of tectonic activity during continental rifting. Tectonophysics, 490 165–172.
Corti, G., Ranalli, G., Agostini, A., Sokoutis, D. 2013. Inward migration of faulting during continental rifting: Effects of pre-existing lithospheric structure and extension rate. Tectonophysics 594, 137-148.
http://dx.doi.org/10.1016/j.tecto.2013.03.028

Corti, G., Bastow, I.D., Keir, D., Pagli, C., Baker, E. 2015(a). Rift-Related Morphology of the Afar Depression. In: Billi, P. (ed.) Landscapes and Landforms of Ethiopia, World Geomorphological Landscapes. Springer Science+Business Media, Dordrecht, 251-274.
doi:10.1007/978-94-017-8026-1_15
Corti, G., Agostini, A., Keir, D., Van Wijk, J., Bastow, I.D., Ranalli, G. 2015(b). Magma-induced axial subsidence during final-stage rifting: Implications for the development of seaward-dipping reflectors. Geosphere 11, 563-571.
doi:10.1130/GES01076.1
Corti, G., Molin, P., Sembroni, A., Bastow, I.D., Keir, D. 2018. Control of pre-rift lithospheric structure on the architecture and evolution of continental rifts: Insights from the Main Ethiopian Rift, East Africa. Tectonics 37, 477-496.
doi:10.1002/2017TC004799
Desissa, M., Johnson, N., Whaler, K., Hautot, S., Fisseha, S., Dawes, G. 2013. A mantle magma reservoir beneath an incipient mid-ocean ridge in Afar, Ethiopia. Nature Geoscience 6, 861–865.
doi:10.1038/ngeo1925
Dooley, T., McClay, K.R., Pascoe, R. 2003. 3D analogue models of variable displacement extensional faults: applications to the Revfallet Fault system, offshore mid-Norway. Geological Society, London, Special Publications 212, 151-167.
http://dx.doi.org/10.1144/GSL.SP.2003.212.01.10
Doubre, C., Déprez, A., Masson, F., Socquet, A., Lewi, E., Grandin, R., Nercessian, A, Ulrich, P., De Chabalier, J.-B., Saad, I., Abayazid, A., Petlzer, G., Delorme, A., Calais, E., Wright, T.

2017. Current deformation in Central Afar and triple junction kinematics deduced from GPS and InSAR measurements, Geophysical Journal International 208, 936–953
doi:10.1093/gji/ggw434
Ebinger, C.J., Hayward, N.J. 1996. Soft plates and hot spots: Views from Afar. Journal of Geophysical Research: Solid Earth 101, 21859– 21876.
doi:10.1029/96JB02118
Ebinger, C., Sleep, N.H. 1998. Cenozoic magmatism in central and east Africa resulting from impact of one large plume. Nature 395, 788–791.
doi:10.1038/27417
FILA 2020. FILA (Fabbrica Italiana Lapis ed Affini) company website: https://www.fila.it/it/en/product/giotto-pongo/
Gabrielsen, R.H., Zalmstra, H., Sokoutis, D., Willingshofer, E., Faleide, J.I., Braut, H.L. 2019. The influence of mechanically weak layers in controlling fault kinematics and graben configurations: Examples from analog experiments and the Norwegian continental margin. AAPG Bulletin 103, 1097–1110.
doi:10.1306/10261817077
Hammond, J.O.S., Kendall, J.-M., Stuart, G.W., Keir, D., Ebinger, C., Ayele, A., Belachew, M. 2011. The nature of the crust beneath the Afar triple junction: Evidence from receiver functions. Geochemistry, Geophysics, Geosystems, 12, Q12004. doi:10.1029/2011GC003738
Hansen, S., Nyblade, A.A. 2013. The deep seismic structure of the Ethiopia/Afar hotspot and the African superplume. Geophysical Journal International 194, 118-124.
doi:10.1093/gji/ggt116
Hardy, S. 2018. Coupling a frictional-cohesive cover and a viscous substrate in a discrete element model: First results of application to thick- and thin-skinned extensional tectonics. Marine and Petroleum Geology 97, 32-44. doi:10.1016/j.marpetgeo.2018.06.026
Hoffmann, C., Courtillot, V., Féraud, G., Rochette, P., Yirgu, G., Ketefo, E., Pik, R. 1997. Timing of the Ethiopian flood basalt event and implications for plume birth and global change. Nature 389, 838-841. doi:10.1038/39853
Illsley-Kemp, F., Keir, D., Bull, J. M., Gernon, T. M., Ebinger, C., Ayele, A., Hammond, J.O.S., Kendall, J.-M., Goitom, B., Belachew, M. 2018. Seismicity during continental breakup in the Red Sea rift of Northern Afar. Journal of Geophysical Research: Solid Earth, 123. doi:10.1002/2017JB014902
Leroy, S., d'Acremont, E., Tiberi, C., Basuyau, C., Autin, J., Lucazeau, F., Sloan, H. 2010. Recent off-axis volcanism in the eastern Gulf of Aden: Implications for plume–ridge interaction. Earth and Planetary Science Letters 293, 140–153.
doi:10.1016/j.epsl.2010.02.036
Lewi, E., Keir, D., Birhanu, Y., Blundy, J., Stuart, G., Wright, T. 2016. Use of a high-precision gravity survey to understand the formation of oceanic crust and the role of melt at the southern Red Sea rift in Afar, Ethiopia. Geological Society, London, Special Publications 420, 165-180.
doi:10.1144/SP420.13
Livio, F., Kettermann, M., Reicherter, K., Urai, J.L. 2019. Growth of bending-moment faults due to progressive folding: Insights from sandbox models and paleoseismological implications. Geomorphology 326, 152-166.
doi:10.1016/j.geomorph.2018.02.012
Mackenzie, G.D., Thybo, H., Maguire, P.K.H. 2005. Crustal velocity structure across the Main Ethiopian Rift: Results from two - dimensional wide - angle seismic modelling, Geophysical Journal International 162, 994–1006.
doi:10.1111/j.1365-246X.2005.02710.x
McCluskey, S., Reilinger, R., Ogubazghi, G., Amleson, A., Healeb, B., Vernant, P., Sholan, J., Fisseha, S., Asfaw, L., Bendick, R., Kogan, L. 2010. Kinematics of the southern Red Sea–Afar Triple Junction and implications for plate dynamics. Geophysical Research Letters 37, L05301.
doi:10.1029/2009GL041127

Mohr, P. 1962. The Ethiopian rift system. Bulletin of the Geophysical Observatory, Addis Ababa 5, 33-62.
Mohr, P. 1983a. Ethiopian flood basalt province. Nature 303, 577-584. doi:10.1038/303577a0
Mohr, P. 1983b. The Morton-Black hypothesis for the thinning of continental crust – revisited in Western AFAR. Tectonophysics, 94, 509-528. doi:10.1016/0040-1951(83)90032-X
Montanari, D., Agostini, A., Bonini, M., Corti, G., Del Ventisette, C. 2017. The Use of Empirical Methods for Testing Granular Materials in Analogue Modelling. Materials 10, 635. doi:10.3390/ma10060635
Morton, W.H., Black, R. 1975. Crustal attenuation in Afar. In: Pilger, A., Roster, A. (eds.) Afar Depression of Ethiopia, Schweizerbart, Stuttgart, 55-61.
Naylor, M.A., Laroque, J.M., Gauthier, B.D.M. 1994. Understanding extensional tectonics: insights from sandbox models. In: Roure, F., Ellouz, N., Shein, V.S., Skvortsov, I.I. (eds). Geodynamic evolution of sedimentary basins. International Symposium on Geodynamic Evolution of Sedimentary Basins, Moscow (Russian Federation). Technip, 92 (France), 69-83.
Norcliffe, J.R., Paton, D.A., Mortimer, E.J., McCaig, A.M., Nicholls, H., Rodriguez, K., Hodgson, N., Van Der Spuy, D. 2018. Laterally confined volcanic successions (LCVS); recording rift-jumps during the formation of magma-rich margins. Earth Planet. Sci. Lett. 504, 53–63.
doi:10.1016/j.epsl.2018.09.033

Pagli, C., Yun, S.-H., Ebinger, C., Keir, D., Wang, H. 2019. Strike-slip tectonics during rift linkage. Geology 47, 31-34.
doi:10.1130/G45345.1
Paton, D.A., Pindell, J., McDermott, K., Bellingham, P., Horn, B. 2017. Evolution of seaward-dipping reflectors at the onset of oceanic crust formation at volcanic passive margins: Insights from the South Atlantic. Geology 45, 439-442
doi:10.1130/G38706.1
Philippon, M., Willingshofer, E., Sokoutis, D., Corti, G., Sani, F., Bonini, M., Cloetingh, S. 2015. Slip re-orientation in oblique rifts. Geology 43, 147-150.
doi:10.1130/G36208.1
Pik, R., Marty, B., Hilton, D.R. 2006. How many mantle plumes in Africa? The geochemical point of view. Chemical Geology 226, 100–114.
doi:10.1016/j.chemgeo.2005.09.016
Purcell, P.G. 2017. Re-imagining and re-imaging the development of the East African Rift. Petroleum Geoscience, 24, 21-40.
doi:10.1144/petgeo2017-036
Rogers, N., Macdonald, R., Godfrey Fitton, J., George R., Smith, M., Barreiro, B. 2000. Two mantle plumes beneath the East African rift system: Sr, Nd and Pb isotope evidence from Kenya Rift basalts. Earth and Planetary Science Letters 176, 387-400.
doi:10.1016/S0012-821X(00)00012-1
Schellart, W.P. 2002. Analogue modelling of large-scale tectonic processes: an introduction. Journal of the Virtual Explorer 7, 1-6.
doi:10.3809/jvirtex.2002.00045
Smith, J.V. 1993. Infinitesimal kinematics of rotational rifting with reference to en echelon marginal faults in the Red Sea region. Tectonophysics 222, 227-235.
doi:10.1016/0040-1951(93)90050-T
Stab, M., Bellahsen, N., Quicelleur, X., Ayalew, D., Leroy, S., 2016. Modes of rifting in magma-rich settings: Tectonomagmatic evolution of Central Afar. Tectonics, 35, 2-38.
doi:10.1002/2015TC003893
Szymanski, E., Stockli, D.F., Johnson, P.R., Hager, C. 2016. Thermochronometric evidence for diffuse extension and two-phase rifting within the Central Arabian Margin of the Red Sea Rift. Tectonics 35, 2863–2895.
doi:10.1002/2016TC004336

Tesfaye, S., Harding, D.J., Kusky, T.M. 2003. Early continental breakup boundary and migration of the Afar triple junction, Ethiopia. GSA Bulletin 115, 1053-1067. doi:10.1130/B25149.1
Tesfaye, S., Ghebreab, W. 2013. Simple shear detachment fault system and marginal grabens in the southernmost Red Sea rift. Tectonophysics 608, 1268–1279. http://dx.doi.org/10.1016/j.tecto.2013.06.014
Tugend, J., Gillard, M., Manatschal, G., Nirrengarten, M., Harkin, C., Epin, M.-E. Sauter, D., Autin, J., Kusznir, N., McDermott, K. 2018. Reappraisal of the magma-rich versus magma-poor rifted margin archetypes. Geological Society, London, Special Publications 476. doi:10.1144/SP476.9

Ukstins, I.A., Renne, P.R., Wolfenden, E., Baker, J., Ayalew, D., Menzies, M. 2002. Matching conjugate volcanic rifted margins: $^{40}Ar/^{39}Ar$ chrono-stratigraphy of pre- and syn-rift bimodal flood volcanism in Ethiopia and Yemen. Earth and Planetary Science Letters 198, 289-306. doi:10.1016/S0012-821X(02)00525-3
Wolfenden, E., Ebinger, C., Yirgu, G., Deino, A., Ayalew, D. 2004. Evolution of the northern Main Ethiopian rift: birth of a triple junction. Earth an Planetary Science Letters 224, 213-228. doi:10.1016/j.epsl.2004.04.022
Wolfenden, E., Ebinger, C., Yirgu, G., Renne, P.R., Kelley, S.P. 2005. Evolution of a volcanic rifted margin: Southern Red Sea, Ethiopia. GSA Bulletin 117, 846-864. doi:10.1130/B25516.1
Zwaan, F., Schreurs, G., Adam, J. 2018. Effects of sedimentation on rift segment evolution and rift interaction in orthogonal and oblique extensional settings: Insights from analogue models analysed with 4D X-ray computed tomography and digital volume correlation techniques. Global and Planetary Change. doi:10.1016/j.gloplacha.2017.11.002
Zwaan, F., Schreurs, G., Buiter, S.J.H. 2019. A systematic comparison of experimental set-ups for modelling extensional tectonics. Solid Earth 10, 1063-1097. doi:10.5194/se-10-1063-2019
Zwaan, F., Corti, G., Keir, D., Sani, F. 2020(a). A review of tectonic models for the rifted margin of Afar: implications for continental break-up and passive margin formation. Journal of African Earth Sciences 164, 103649 doi:10.1016/j.jafrearsci.2019.103649
Zwaan, F., Corti, G., Sani, F., Keir, D., Muluneh, A., Papini, M. 2020(b). Structural analysis of the Western Afar Margin, East Africa: evidence for multiphase rotational rifting. Tectonics 39, e2019TC006043. doi:10.1029/2019TC006043
Zwaan, F., Rudolf, M., Pohlenz, A., Corti, G., Keir, D., Sani, F. 2020(c). Ring-shear test data of feldspar sand from the CNR-IGG Tectonic Modelling Laboratory at the University of Florence (Italy), GFZ Data Services. doi:10.5880/fidgeo.2020.019
**NB: DOI nor active yet, temporary link:**
http://pmd.gfz-potsdam.de/panmetaworks/review/25656531adc4a0de794fd05a02ca89b5816a799040d63bbfbb5cba2861f34f48
Zwaan, F., Rudolf, M., Corti, G., Keir, D., Sani, F. 2020(d). Rheology of viscous materials from the CNR Tectonic Laboratory at the University of Florence (Italy), GFZ Data Services. doi:10.5880/fidgeo.2020.018
**NB: DOI nor active yet, temporary link:**
http://pmd.gfz-potsdam.de/panmetaworks/review/f4ab2e1f3b0985fabf6014682ebf5f85b266765e4afb659eefce693b11f19130/
Zwaan, Frank; Corti, G., Keir, D., Sani, F. 2020(e). Images and videos of analogue centrifuge models exploring marginal flexure during rifting in Afar, East Africa, GFZ Data Services. doi:10.5880/fidgeo.2020.020
**NB: DOI nor active yet, temporary link:**

http://pmd.gfz-potsdam.de/panmetaworks/review/89baf63d9c48c173d1d1f2432f2dbb0dcc6b2a457299c2cec542a2f487c9c433/

**CrediT author statement TECTO14201R1**

**Frank Zwaan:**
Conceptualization, Methodology, Investigation, Writing – Original Draft, Visualization, Validation, Data Curation, Funding Acquisition, Project Administration.

**Giacomo Corti:**
Conceptualization, Methodology, Writing - Review & Editing, Resources, Project Administration.

**Derek Keir:**
Conceptualization, Writing - Review & Editing

**Federico Sani:**
Writing - Review & Editing, Resources.

**Definitions:**
https://www.elsevier.com/authors/journal-authors/policies-and-ethics/credit-author-statement

**Highlights WAM modelling paper for Tectonophysics**
**(max 85 characters, incl. spaces, per highlight)**

- Centrifuge analogue models simulate faulting and crustal flexure during extension
- Flexure first forms large escarpments, then antithetic faults and marginal grabens
- Crustal flexure explains the structural architecture of the Western Afar Margin
- Yet only (near-)orthogonal extension allows marginal graben formation
- These results suggest that two tectonic phases shaped the Western Afar Margin

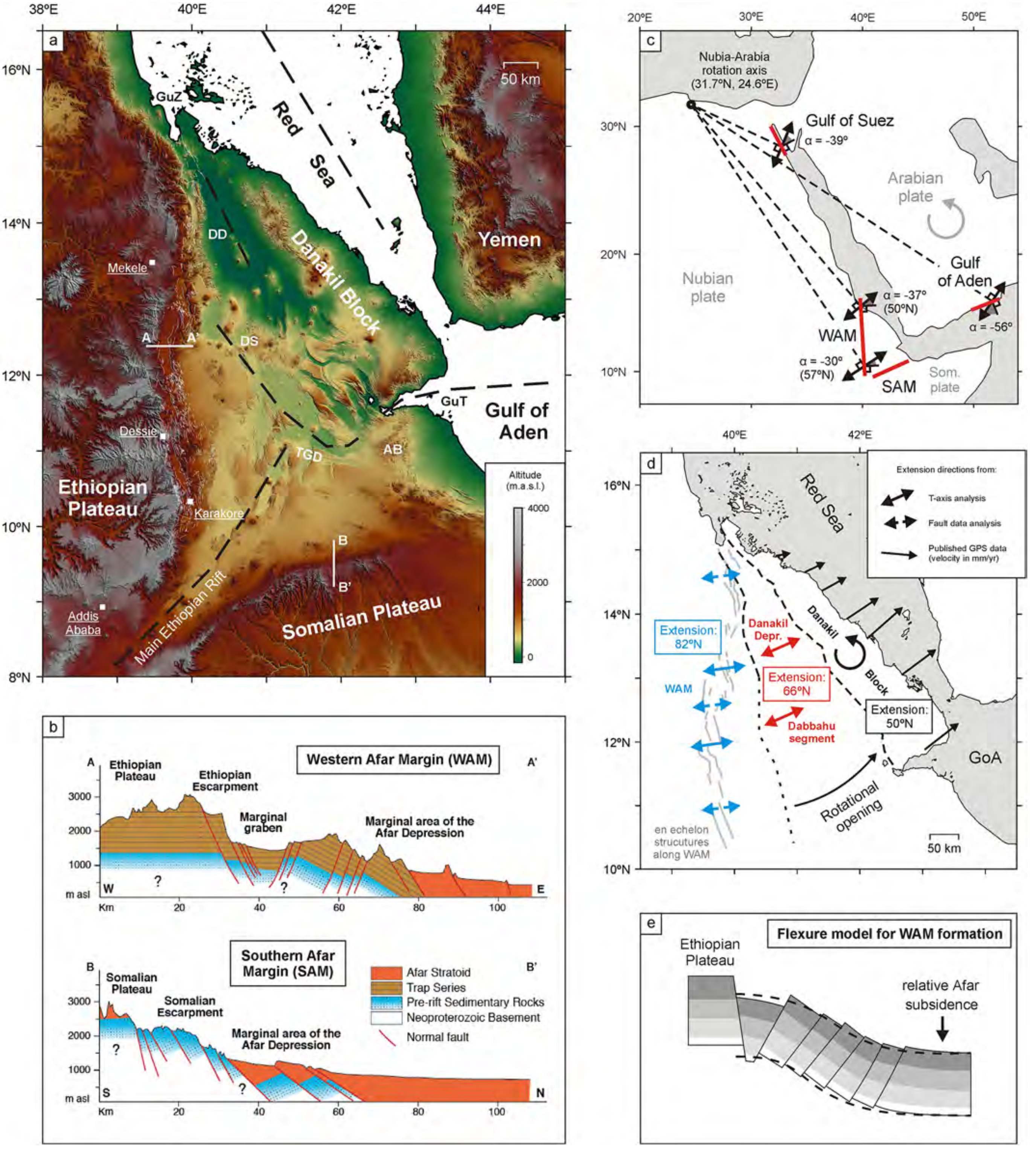
a
Red Sea
Yemen
Danakil Block
Gulf of Aden
Ethiopian Plateau
Somalian Plateau
Main Ethiopian Rift
GuZ
DD
DS
TGD
AB
GuT
Mekele
Dessie
Karakore
Addis Ababa
50 km
Altitude (m.a.s.l.)
b
Western Afar Margin (WAM)
Ethiopian Plateau
Ethiopian Escarpment
Marginal graben
Marginal area of the Afar Depression
Southern Afar Margin (SAM)
Somalian Plateau
Somalian Escarpment
Afar Stratoid
Trap Series
Pre-rift Sedimentary Rocks
Neoproterozoic Basement
Normal fault
c
Nubia-Arabia rotation axis (31.7ºN, 24.6ºE)
Gulf of Suez
α = -39º
Arabian plate
Nubian plate
Gulf of Aden
α = -37º (50ºN)
α = -56º
α = -30º (57ºN)
WAM
SAM
Som. plate
d
Extension directions from:
T-axis analysis
Fault data analysis
Published GPS data (velocity in mm/yr)
Red Sea
Danakil Block
Danakil Depr.
Extension: 82ºN
Extension: 66ºN
Extension: 50ºN
Dabbahu segment
WAM
GoA
Rotational opening
en echelon strucutures along WAM
50 km
e
Flexure model for WAM formation
Ethiopian Plateau
relative Afar subsidence

Figure 1

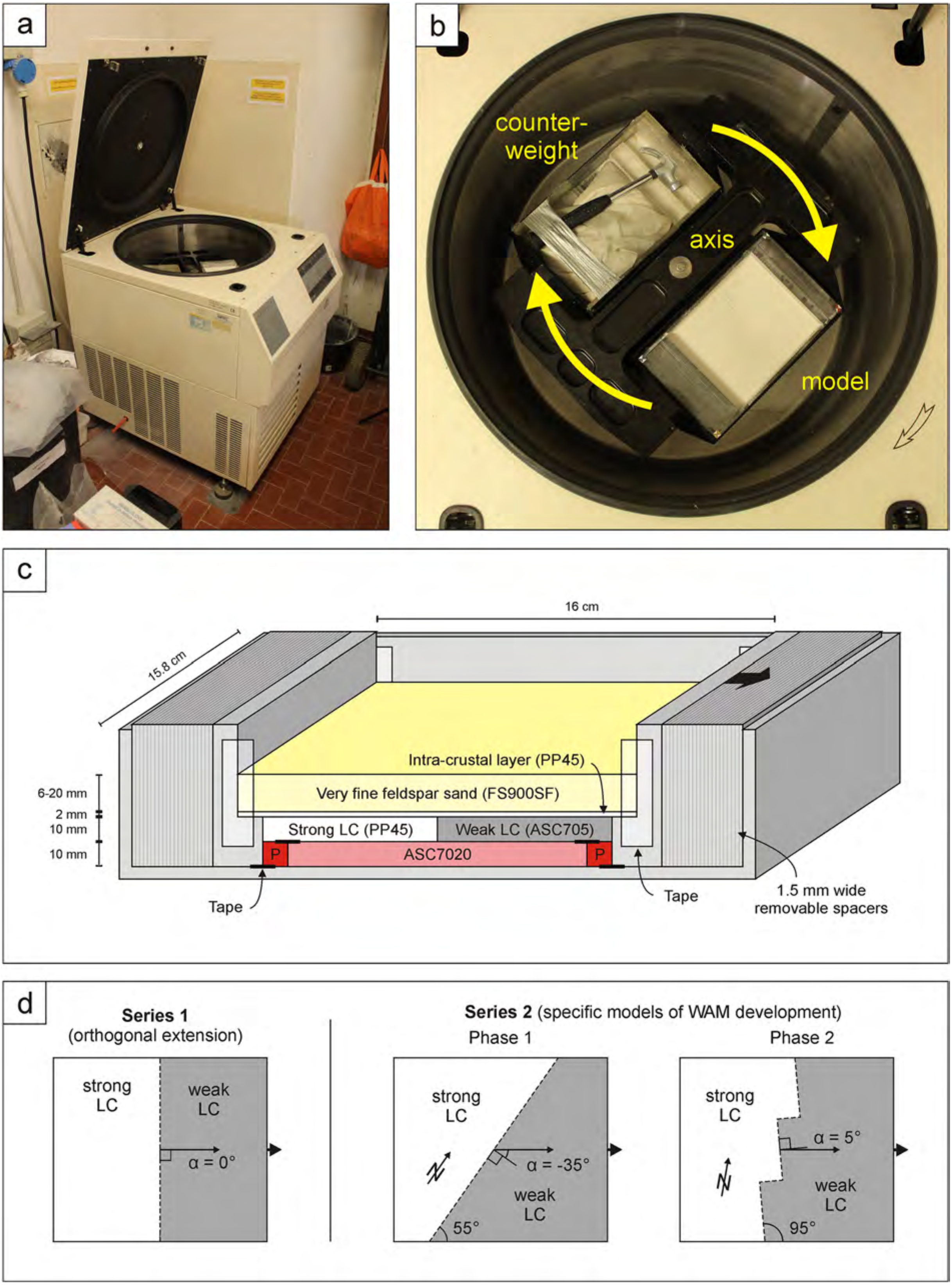
a
b
counter-weight
axis
model
c
16 cm
15.8 cm
6-20 mm
2 mm
10 mm
10 mm
Intra-crustal layer (PP45)
Very fine feldspar sand (FS900SF)
Strong LC (PP45)
Weak LC (ASC705)
ASC7020
P
P
Tape
Tape
1.5 mm wide removable spacers
d
Series 1 (orthogonal extension)
strong LC
weak LC
α = 0°
Series 2 (specific models of WAM development)
Phase 1
strong LC
α = -35°
weak LC
55°
Phase 2
strong LC
α = 5°
weak LC
95°

Figure 2

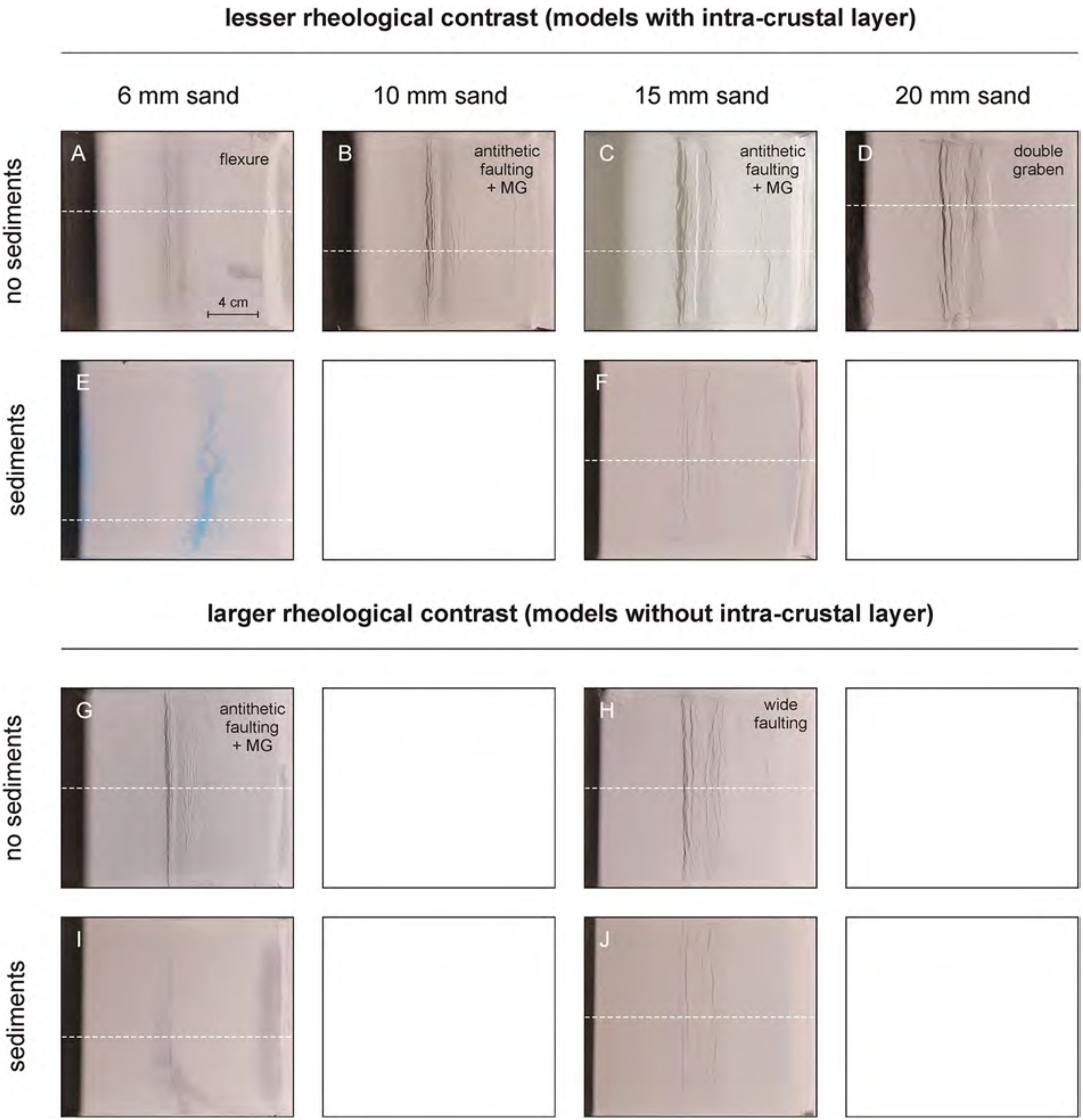
lesser rheological contrast (models with intra-crustal layer)
6 mm sand
10 mm sand
15 mm sand
20 mm sand
no sediments
sediments
A
flexure
4 cm
B
antithetic faulting + MG
C
antithetic faulting + MG
D
double graben
E
F
larger rheological contrast (models without intra-crustal layer)
no sediments
sediments
G
antithetic faulting + MG
H
wide faulting
I
J

Figure 3

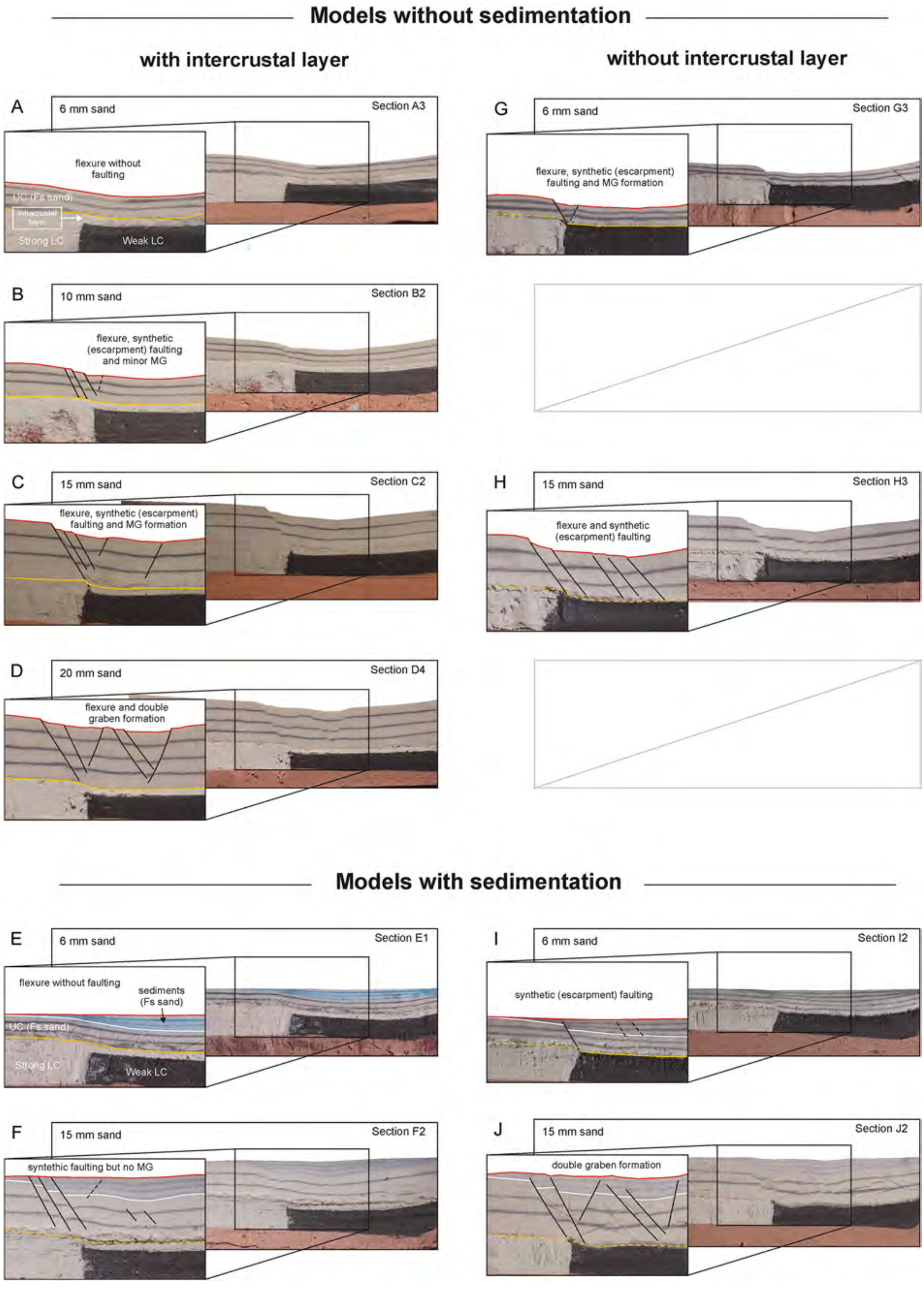
Models without sedimentation
with intercrustal layer
without intercrustal layer
A
6 mm sand
Section A3
flexure without faulting
UC (Fs sand)
intracrustal layer
Strong LC
Weak LC
B
10 mm sand
Section B2
flexure, synthetic (escarpment) faulting and minor MG
C
15 mm sand
Section C2
flexure, synthetic (escarpment) faulting and MG formation
D
20 mm sand
Section D4
flexure and double graben formation
G
6 mm sand
Section G3
flexure, synthetic (escarpment) faulting and MG formation
H
15 mm sand
Section H3
flexure and synthetic (escarpment) faulting
Models with sedimentation
E
6 mm sand
Section E1
flexure without faulting
sediments (Fs sand)
UC (Fs sand)
Strong LC
Weak LC
F
15 mm sand
Section F2
synthethic faulting but no MG
I
6 mm sand
Section I2
synthetic (escarpment) faulting
J
15 mm sand
Section J2
double graben formation

Figure 4


Models with intra-crustal layer
Models without intra-crustal layer
6 mm sand
15 mm sand
6 mm sand
15 mm sand
A
C
G
H
4 cm
t = 0
(0 mm)
t = 1
(1.5 mm)
synthetic
escarpment
faults form
synthetic
escarpment
faults form
t = 2
(3.0 mm)
flexure
starts
synthetic
escarpment
faults form
t = 3
(4.5 mm)
distributed
faulting
appears
marginal
graben
develops
antithetic
faulting
starts
t = 5
(7.5 mm)
marginal
graben
develops
syntethic
faulting
migrates
basinward
t = 7
(10.5 mm)

Figure 5

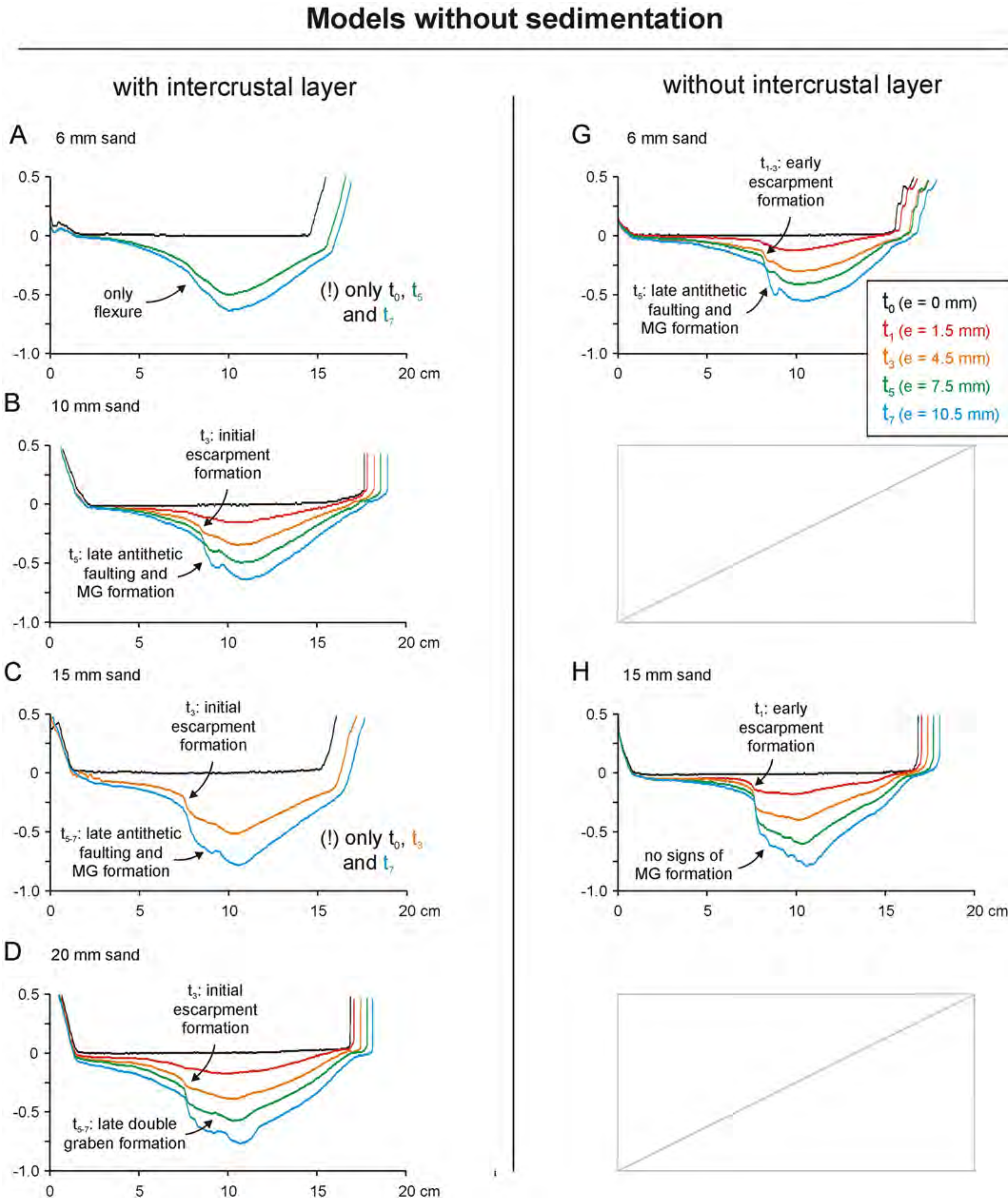
Models without sedimentation
with intercrustal layer
without intercrustal layer
A
6 mm sand
only flexure
(!) only t0, t5 and t7
B
10 mm sand
t3: initial escarpment formation
t5: late antithetic faulting and MG formation
C
15 mm sand
t3: initial escarpment formation
t5-7: late antithetic faulting and MG formation
(!) only t0, t3 and t7
D
20 mm sand
t3: initial escarpment formation
t5-7: late double graben formation
G
6 mm sand
t1-3: early escarpment formation
t5: late antithetic faulting and MG formation
t0 (e = 0 mm)
t1 (e = 1.5 mm)
t3 (e = 4.5 mm)
t5 (e = 7.5 mm)
t7 (e = 10.5 mm)
H
15 mm sand
t1: early escarpment formation
no signs of MG formation
0.5
0
-0.5
-1.0
0
5
10
15
20 cm

Figure 6A

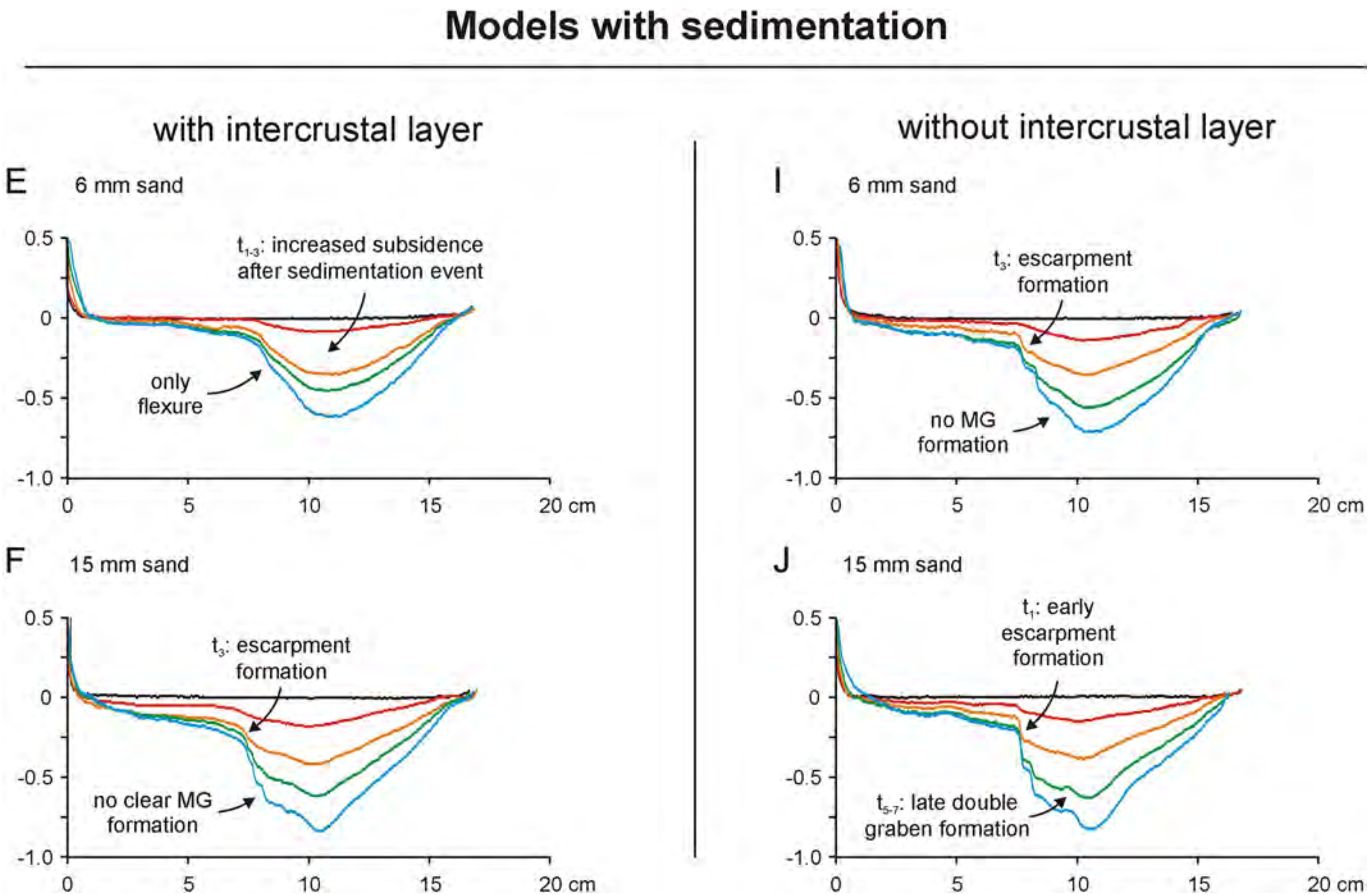
Models with sedimentation
with intercrustal layer
without intercrustal layer
E
6 mm sand
t1-3: increased subsidence
after sedimentation event
only
flexure
I
6 mm sand
t3: escarpment
formation
no MG
formation
F
15 mm sand
t3: escarpment
formation
no clear MG
formation
J
15 mm sand
t1: early
escarpment
formation
t5-7: late double
graben formation
0.5
0
-0.5
-1.0
0
5
10
15
20 cm

Figure 6B

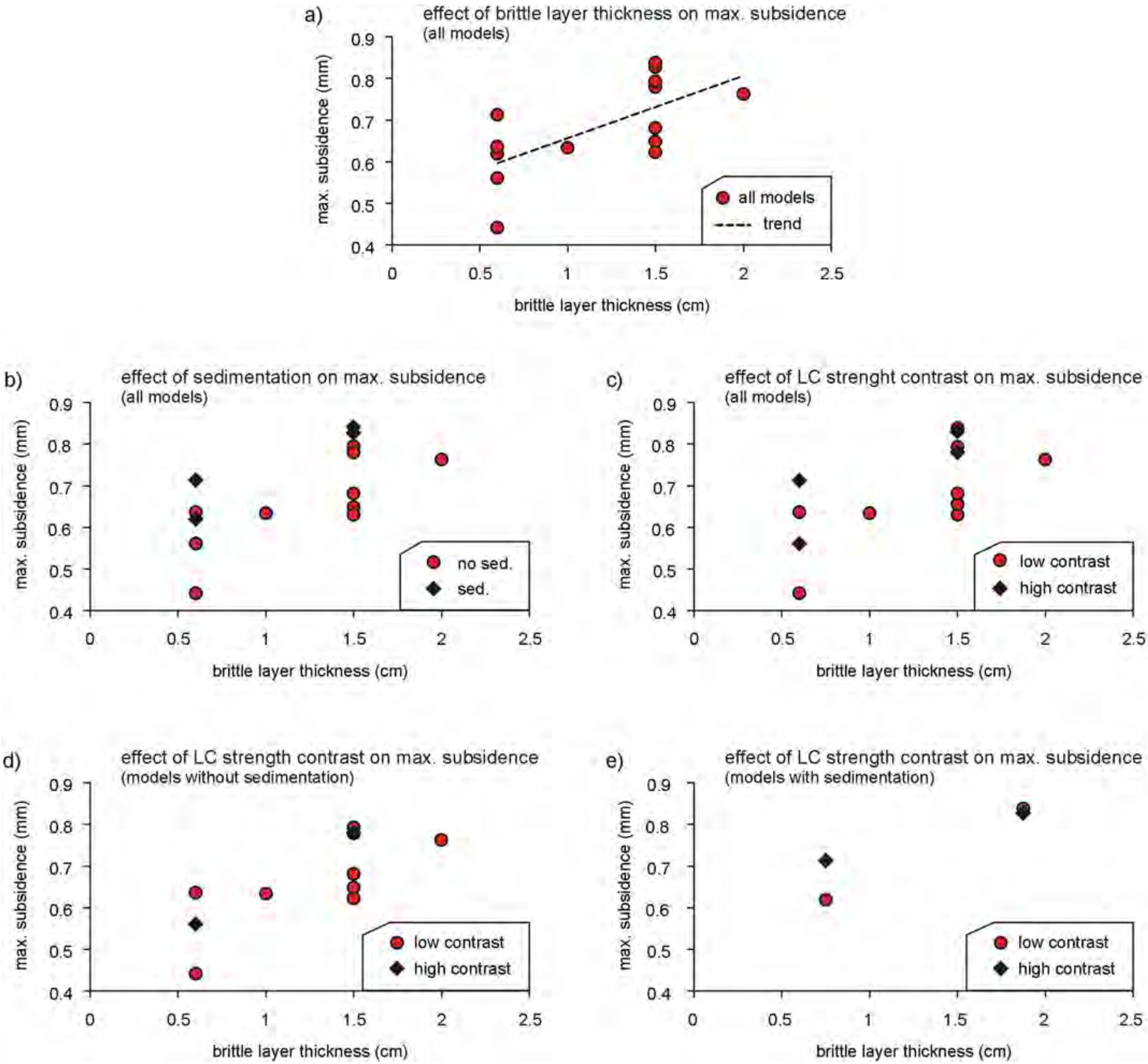
a)
effect of brittle layer thickness on max. subsidence
(all models)
max. subsidence (mm)
brittle layer thickness (cm)
all models
trend
b)
effect of sedimentation on max. subsidence
(all models)
no sed.
sed.
c)
effect of LC strenght contrast on max. subsidence
(all models)
low contrast
high contrast
d)
effect of LC strength contrast on max. subsidence
(models without sedimentation)
e)
effect of LC strength contrast on max. subsidence
(models with sedimentation)

Figure 7

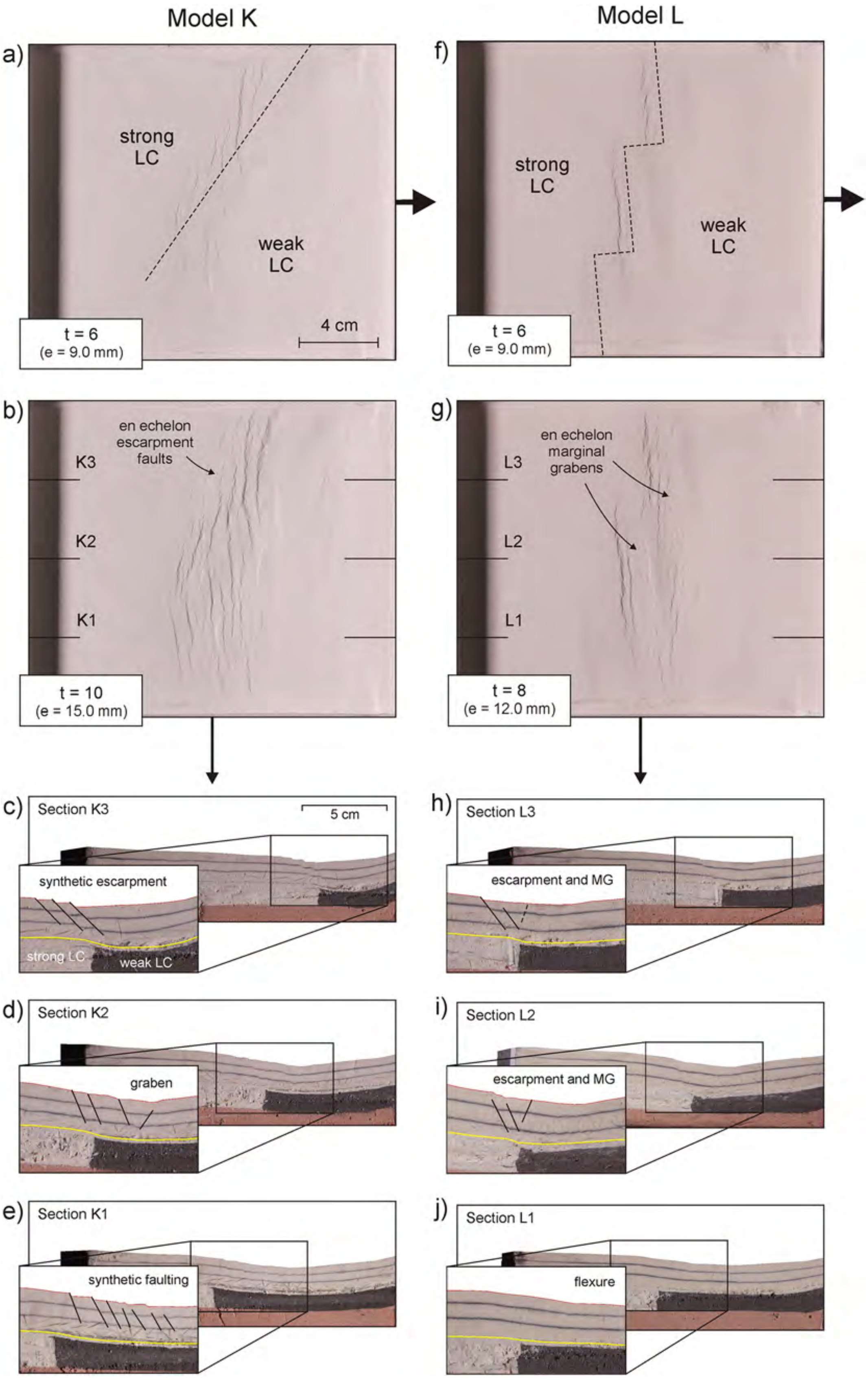
Model K
Model L
a)
strong
LC
weak
LC
t = 6
(e = 9.0 mm)
4 cm
f)
strong
LC
weak
LC
t = 6
(e = 9.0 mm)
b)
en echelon
escarpment
faults
K3
K2
K1
t = 10
(e = 15.0 mm)
g)
en echelon
marginal
grabens
L3
L2
L1
t = 8
(e = 12.0 mm)
c)
Section K3
5 cm
synthetic escarpment
strong LC
weak LC
h)
Section L3
escarpment and MG
d)
Section K2
graben
i)
Section L2
escarpment and MG
e)
Section K1
synthetic faulting
j)
Section L1
flexure

Figure 8

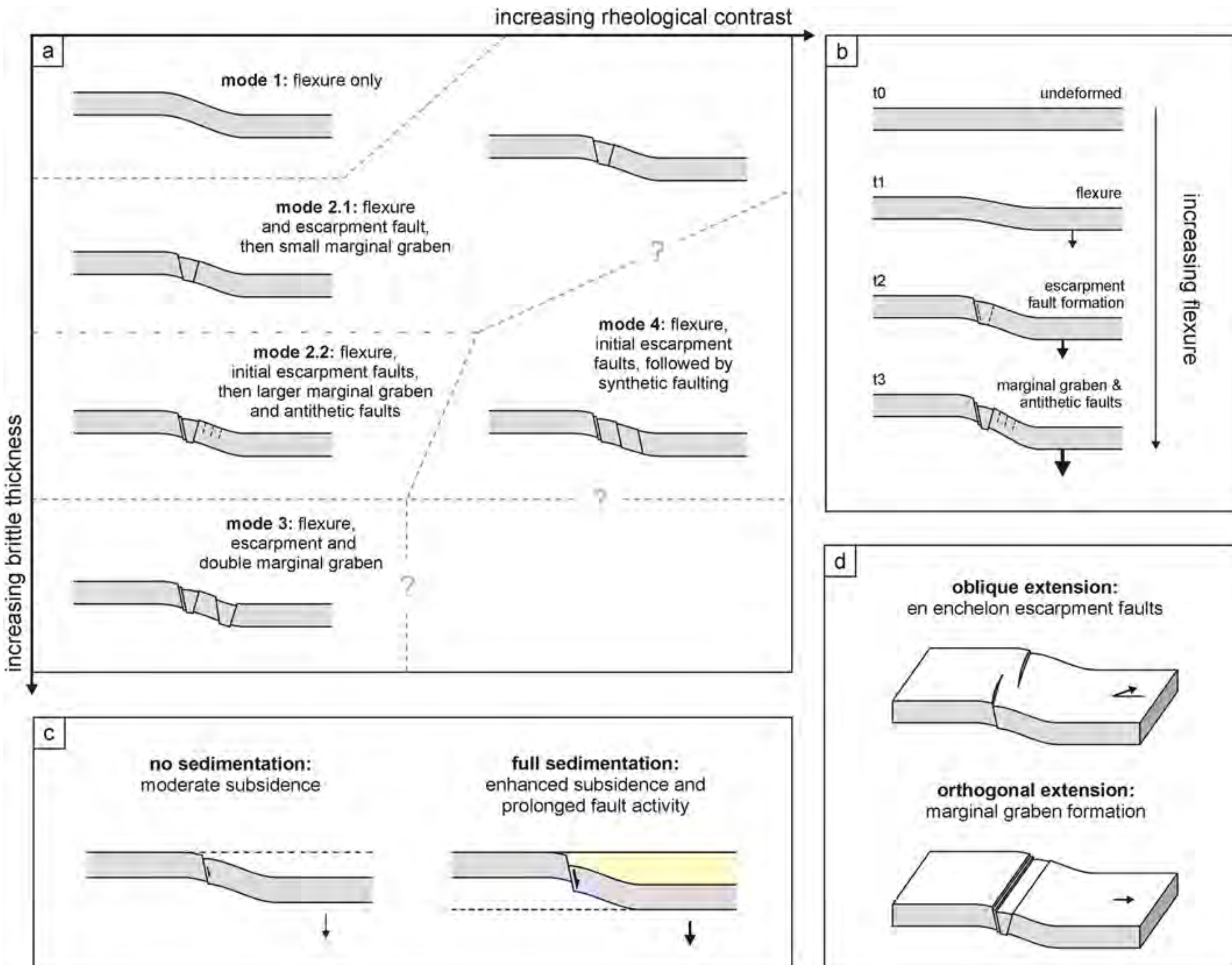
increasing rheological contrast
increasing brittle thickness
a
mode 1: flexure only
mode 2.1: flexure and escarpment fault, then small marginal graben
mode 2.2: flexure, initial escarpment faults, then larger marginal graben and antithetic faults
mode 3: flexure, escarpment and double marginal graben
mode 4: flexure, initial escarpment faults, followed by synthetic faulting
?
?
?
b
t0
undeformed
t1
flexure
t2
escarpment fault formation
t3
marginal graben & antithetic faults
increasing flexure
c
no sedimentation: moderate subsidence
full sedimentation: enhanced subsidence and prolonged fault activity
d
oblique extension: en enchelon escarpment faults
orthogonal extension: marginal graben formation

Figure 9

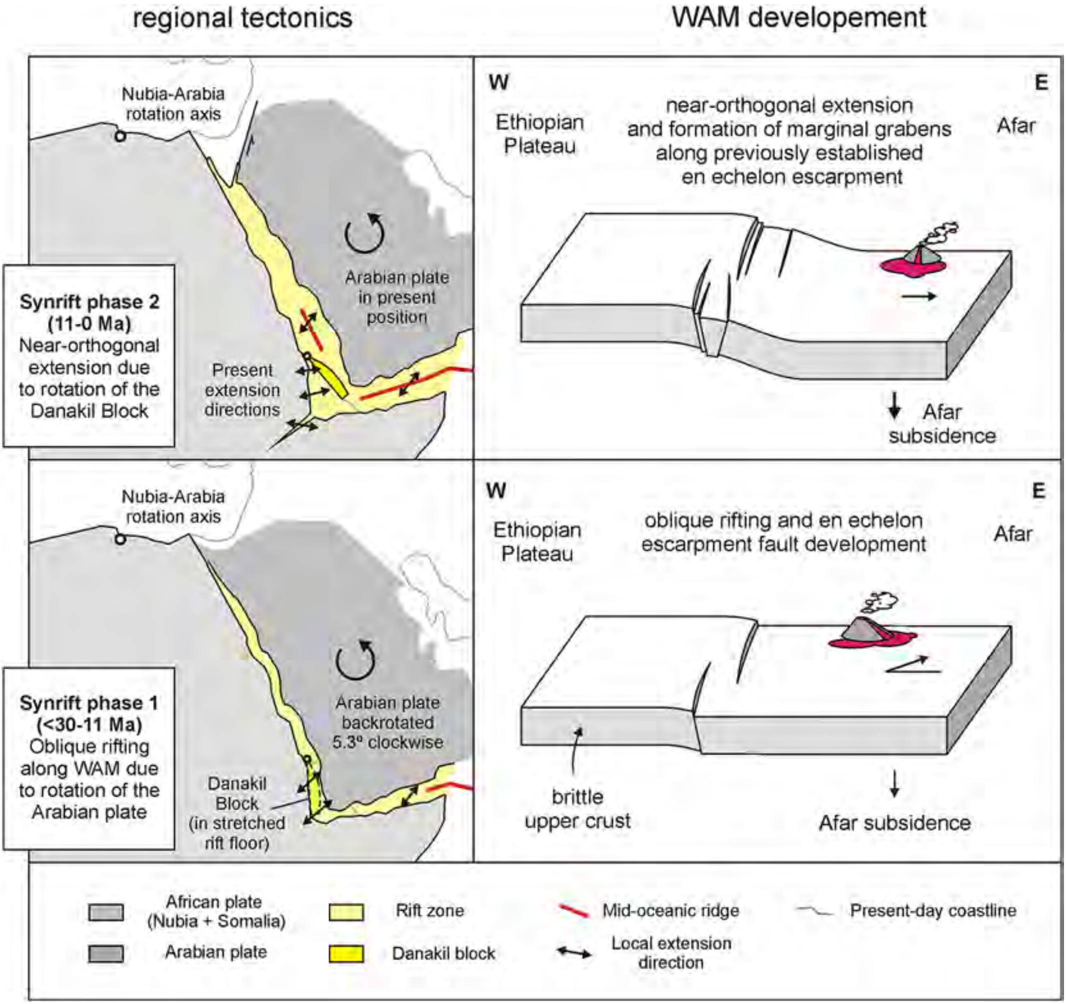
regional tectonics
WAM developement
Nubia-Arabia rotation axis
Arabian plate in present position
Synrift phase 2 (11-0 Ma)
Near-orthogonal extension due to rotation of the Danakil Block
Present extension directions
W
E
Ethiopian Plateau
near-orthogonal extension and formation of marginal grabens along previously established en echelon escarpment
Afar
Afar subsidence
Nubia-Arabia rotation axis
Arabian plate backrotated 5.3° clockwise
Synrift phase 1 (<30-11 Ma)
Oblique rifting along WAM due to rotation of the Arabian plate
Danakil Block (in stretched rift floor)
W
E
Ethiopian Plateau
oblique rifting and en echelon escarpment fault development
Afar
brittle upper crust
Afar subsidence
African plate (Nubia + Somalia)
Arabian plate
Rift zone
Danakil block
Mid-oceanic ridge
Local extension direction
Present-day coastline

Figure 10

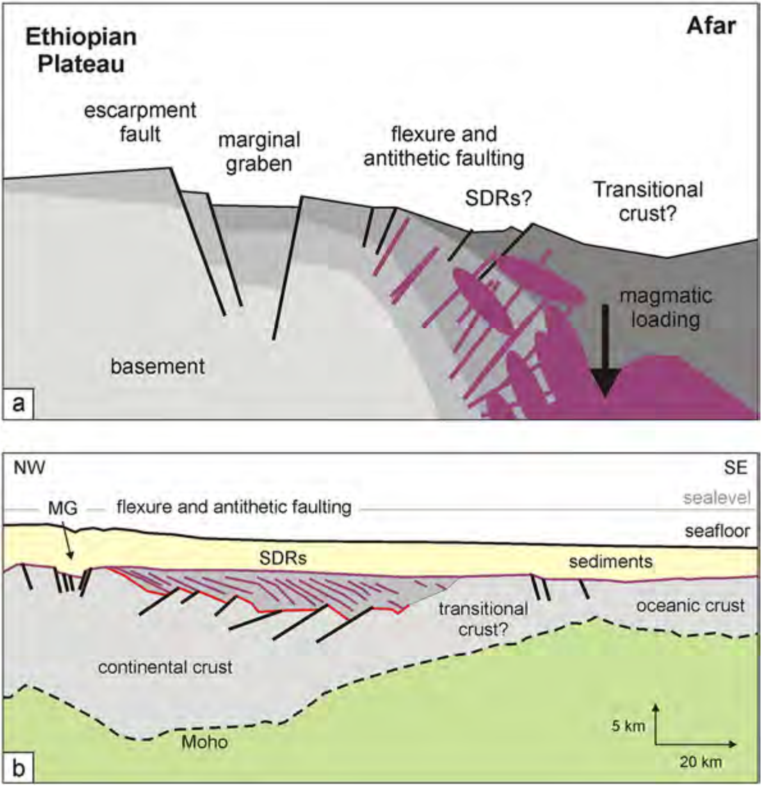

Ethiopian Plateau
Afar
escarpment fault
marginal graben
flexure and antithetic faulting
SDRs?
Transitional crust?
magmatic loading
basement
a
NW
SE
sealevel
MG
flexure and antithetic faulting
seafloor
SDRs
sediments
transitional crust?
oceanic crust
continental crust
Moho
5 km
20 km
b


Figure 11